Cryo-electron microscopy structures of a high-affinity zinc ABC transporter

Changxu Pang[1], Hoang Nguyen[2,3], Qingfang Zhang[2], Ivet Bahar[2,3], Qun Liu[1,2,4]*

[1]Biology Department, Brookhaven National Laboratory; Upton, NY 11973, USA

[2]Department of Biochemistry and Cell Biology, Renaissance School of Medicine, Stony Brook University, Stony Brook, NY 11794, USA

[3]The Laufer Center for Physical and Quantitative Biology, Stony Brook University, Stony Brook, NY 11794, USA

[4]NSLS-II, Brookhaven National Laboratory, Upton, NY 11973, USA.

*Corresponding author. Email: qunliu@bnl.gov

Abstract: How do bacteria acquire scarce Zn^{2+} to fuel vital cellular functions? Microorganisms employ high-affinity Zn^{2+} ABC transporters, yet their structures and regulation are poorly understood. Here, we report cryo-EM structures of the *Escherichia coli* ZnuB–ZnuC complex, revealing a ZnuB homodimer in an outward-facing, sealed conformation with a central hydrophilic cavity and ZnuC subunits composed of an N-terminal ATP-binding cassette and a C-terminal zinc-sensing domain (ZSD). Zn^{2+} binding to the ZSD locks the transporter in an inhibited state regardless of nucleotide, whereas under low–Zn^{2+} conditions, ZSD C-terminal disorder permits ATP-driven zinc uptake. These findings clarify the molecular basis of Zn^{2+} acquisition and highlight new targets for disrupting metal homeostasis in pathogens.

Introduction

The zinc ion (Zn^{2+}) is an essential micronutrient supporting all living organisms. It plays physiological functions in gene transcription, structure rigidity, development, photosynthesis, immune response, and numerous Zn^{2+}-dependent enzymatic activities (*1*). Zn^{2+} is impermeable to membranes and has to be transported across cell membranes by Zn^{2+} uptake transporters including Zrt-/Irt-like proteins (ZIPs) (*2, 3*), ATP-binding cassette (ABC) transporters(*4*), and natural resistance-associated macrophage proteins (NRAMP)(*5*) before being used by cells. While Zn^{2+} is an essential micronutrient, nevertheless, its excessive accumulation is cytotoxic, and its intracellular concentration has to be tightly regulated. As revealed by ^{65}Zn uptake assays, Zn^{2+} ABC transporters are high-affinity transporters whose expression levels are tightly regulated by the Zn^{2+}-sensing transcription factor Zur (*6*). Many bacterial pathogens use ABC transporters to compete for Zn^{2+} with their hosts - humans, animals, and plants. Conversely, upon sensing a pathogen attack, the hosts produce Zn^{2+}-chelating proteins and molecules to limit the access of Zn^{2+} to be used by pathogens, forming an adaptive immunity called nutritional immunity (*7-16*). These pathogen-specific ABC transporters may be attractive targets for the development of novel antibiotics and vaccines. However, the structure and mechanism of function of Zn^{2+} ABC transporters, and how their activities are regulated and linked to intracellular Zn^{2+} contents, remain largely unclear.

ABC transporters are a large family of transporters ubiquitous among all living organisms. They use ATP hydrolysis to drive the transport of ions, metabolites, proteins, nucleotides, and other biological molecules across membranes (*17, 18*). Many human ABC transporters are also important drug targets for diseases (*17*). The ABC transporters contain at least two ATP-binding cassette (ABC) domains (also called nucleotide-binding domains, NBDs) and two transmembrane (TM) domains (TMD). The NBD regulates the transport activity in the TMD through ATP binding and hydrolysis. ZnuABC is an *E. coli* ABC transporter; it is composed of five subunits: two transmembrane (ZnuB) subunits, two ATP-binding cassette (ABC) regulatory (ZnuC) subunits, and one Zn^{2+} binding protein substrate (ZnuA)(*19*). In this work, we employ cryo-electron microscopy (cryoEM) to investigate the structures of ZnuB-ZnuC (named as ZnuBC) complex, from which to draw insights into the Zn^{2+} uptake and regulation mechanism.

Results

Structure determination

The expression of *ZnuA, ZnuB, and ZnuC* in *E. coli* is regulated by the *zur* transcription factor, as illustrated in **Fig. S1a**. We cloned the *E. coli ZnuA and ZnuBC* genes into the pETDuet1 vector with one cassette containing *ZnuBC* and the other cassette containing *ZnuA* (**Fig. S1b**). We expressed the complex in bacteria, purified it in detergent, and reconstituted it into amphipol nanodiscs using a workflow summarized in **Fig. S1c**. The complex contained ZnuB and ZnuC (ZnuBC), lacking ZnuA (**Fig. S1d**). We verified that the reconstituted ZnuBC complex is active in hydrolyzing ATP (**Fig. S1e**) and determined its structure using single-particle cryoEM. The reconstructed 3D map shows a belt of amphipol densities around the ZnuB transporter protruded by the ZnuC dimer (**Fig. 1a**). To obtain the structure, we prepared the ZnuBC particles (**Fig. S2a**) in the presence of adenylyl-imidodiphosphate (AMP-PNP), a nonhydrolyzing ATP analog. Averaged 2D classes showed multiple views of a 2-fold dimer (**Fig. S2b**). The structure solution workflow is summarized in **Fig. S3**. The reconstructed cryoEM map used 34,187 particles, reaching a resolution of 2.5 Å resolution (**Fig. S4a**). The final reconstruction contains particles with a widespread distribution in Euler space with slightly more views at elevation angles around

zero (**Fig. S5a**). The cryoEM density is of high quality, showing all nine transmembrane helices and most side-chain features in a transporter subunit (**Fig. S6**).

Overall structure

The ZnuBC structure is a heterotetramer, consisting of two copies of ZnuB and ZnuC subunits (**Fig. 1b-c**). ZnuB is the zinc transporter subunit. The two ZnuB subunits form a dimer with an interface of 1503 $Å^2$ as calculated by PISA (*20*). Each ZnuB monomer contains nine TM helices (TM1-TM9) and two short α-helices: α1 in the periplasm and α2 in the cytosol (**Fig. 1c, d**). Most TM helices are bent or tilted inside the membrane. TM5 is long and extends from the membrane into the cytosol, followed by α2, which is known as a coupling helix in ABC transporters (*18*). TM6 and TM7 do not fully cross the membrane; they form a kink inside the membrane. The intramembrane loop between TM6 and TM7, L(6,7), has close contact with the periplasmic helix α1, which connects to TM4 and TM5 through two long loops (**Fig. 1d**). ZnuC is the regulatory subunit, located in the cytosol. It interacts with ZnuB mainly through the α2 on ZnuB and a Q loop on ZnuC. The two ZnuC monomers form an interface of 1606 $Å^2$. They each contain an AMP-PNP molecule bound to their NBD. The C-terminus of ZnuC has an extended domain consisting of three β-strands (β11-13), two short α-helices (α6 and α7), and a long loop. Surprisingly, the extension harbors two Zn^{2+} ions in each of the ZnuC subunits (**Fig. 1c, e**).

ZnuB zinc transporter

The ZnuB dimer has a two-fold symmetry; TM2, TM4, TM7, and TM9 from each monomer form the dimer interface (**Fig. 2a, b**). A 40 Å-long transport channel from the periplasmic side to the cytosol is at the dimer interface (**Fig. 2c, d**), lined by TM2 and TM4 residues of each subunit. These two helices on each ZnuB subunit bend to expose a vestibule to the periplasm with the α1 helices inserted as a plug to constrict the channel. Therefore, we interpret this structure as an outward-facing inhibited state. The channel is wide in the middle and has two restriction bottlenecks. On the periplasmic side, the bottleneck is formed by the hydrophobic residues Met112, Leu115, and Phe116 from α1 and Leu190 from the loop L(6,7). On the cytosol side, the bottleneck is formed mainly by Tyr33 residues from both subunits.

Between the two bottlenecks, there is a large cavity. The cavity is hydrophobic on the periplasmic side, formed by residues Leu94 and Leu190 (**Fig. 2d**). The hydrophobic residues may help seal the transporter to prevent a leak of Zn^{2+}. The cytoplasmic side is hydrophilic, formed by conserved residues Asp36, His40, and less conserved residue His91 (**Fig. 2e**, **Fig. S7**). The cavity is elongated and has enough space to accommodate one Zn^{2+} inside. We hypothesized that the side chains of the conserved Asp36 and His40 might contribute to the Zn^{2+} transport activity. We thus produced D36A, H40A, and D36A-H40A mutants, transformed them with bacterial cells, and measured cell growth viability under Ethylenediaminetetraacetic acid (EDTA) treatment (**Fig. 2f, and Fig. S8a**). EDTA removed Zn^{2+} from uptake by bacteria. Compared to the plasmid control and wild-type (WT), the D36A-H40A double mutant did not grow well under Zn^{2+}-limiting conditions (treated with 2 mM EDTA). The D36A and H40A single mutants could still support bacteria growth under EDTA treatment, suggesting that His91, which is less conserved in the large majority of pathogenic ZnuB sequences (**Fig. S7**), may also contribute to Zn^{2+} uptake. To test if His91 is involved in the ZnuB transport function, we produced H91A, D36A-H91A, and H40A-H91A mutants and performed cell viability assays in the presence of various concentrations of EDTA (**Fig. S8b**), we found that cells overexpressing H91A grown similarly to the wild-type; D36A-H91A and H40A-H191A double mutants remain active in Zn^{2+} uptake, suggesting that His91 is not as important as Asp36 and His40 in Zn^{2+}

transport. In addition, bacterial cells transformed with WT grew better than the control under the Zn^{2+}-limiting condition, implicating that ZnuB was expressed and contributed to the uptake of Zn^{2+} from the Zn^{2+}-limiting environment.

ZnuC nucleotide-binding cassette

ZnuC is the regulatory subunit of the Zn^{2+} ABC transport system. It has two domains, the NBD at the N-terminus and the Zn^{2+} sensing domain (ZSD) at the C-terminus (**Fig. 3a, b**). The NBD contains five α-helices and 11 β-strands. In the NBD, two β-sheets sandwich the α1 helix. The AMP-PNP molecule binds at the N-terminus of α1. In ABC transporters, ATP or AMP-PNP binding triggers dimerization through an ATP (*21*). However, in the ZnuC dimer structure, AMP-PNP has no interactions with the other ZnuC subunit, indicating not involved in dimerization (**Fig. 3a, c, Fig. S9a**). We also produced an ATPase-deficient E146Q mutant and solved its cryoEM structure in the presence of ATP at 2.9 Å resolution (**Fig. S4b,5b**). The solved structure is similar to the AMP-PNP-bound structure, and neither ATP molecules is involved in the dimerization of ZnuC (**Fig. S9b**).

AMP-PNP binds the NBD primarily via the Walker A motif (**Fig. 3c**). Its phosphate groups form hydrogen bonds with Gly42, Gly43 and Thr45, while Ser44 and two phosphate oxygens coordinate the Mg^{2+} ion that is also liganded by Glu74 in the Q-loop (residues 74–85). The side chain of the Walker B catalytic residue, Glu146, points directly at the γ-phosphate, positioning it for hydrolysis. Meanwhile, the adenine ring of AMP-PNP π-stacks against Phe14 in β2. All of these contacts are retained in the ATP-bound E146Q mutant structure (**Fig. S9a,b**).

To assess nucleotide-induced changes, we solved an apo-form, nucleotide-free cryo-EM structure (**Fig. S4c, S5c**) and overlaid it with the AMP-PNP–bound model. ZnuB, including coupling helix α2, shows virtually no shift (RMSD 0.337 Å over 260 Cα atoms), and ZnuC also remains largely unchanged (RMSD 0.455 Å over 242 Cα atoms) (**Fig. 3d**). The only notable differences localize to the nucleotide pocket: side-chain reorientations of Gln74, Phe14 in β2, and movement of the L(3,4) loop. Importantly, the Q-loop backbone itself is unaltered. Thus, ATP binding at the Walker A site does not trigger significant global rearrangements in either ZnuB or ZnuC.

ZnuC Zn^{2+} binding and autoinhibition

It is surprising that AMP-PNP binding produces no large-scale rearrangements in the ZnuBC complex. In both the apo and nucleotide-bound structures, the ZnuC zinc-sensing domain (ZSD) harbors two Zn^{2+} sites, M1 and M2 (**Fig. 4a, S9c**). M1 is coordinated by Cys193, Cys200, His230 and His232; M2 by His197, Cys199, His234 and His246. These two Zn^{2+} ions lock the ZSD C-terminus into a rigid conformation, and helices α6–α7 from each monomer pack tightly to form a dimer interface burying ~807 $Å^2$. This Zn^{2+}-stabilized interface likely prevents the global ATP-induced conformational switch, confining movement to local side-chain shifts around the nucleotide pocket (**Fig. 3d**).

We therefore asked whether M1 and M2 act as intracellular Zn^{2+} sensors to autoregulate transport. We replaced each coordinating Cys/His with alanine, expressed the mutants in *E. coli*, and compared growth in media containing 0 or 1 mM Zn^{2+} (**Fig. S10**). The M2 mutant behaved like wild type, but both the M1 and M1M2 double mutants showed markedly reduced viability under high Zn^{2+}, consistent with loss of regulation leading to toxic Zn^{2+} accumulation.

Finally, we identified a strictly conserved motif, Cys193xxxHisxxCysCys204, in 5,712 ZnuC homologs, including major human and plant pathogens, using PatternSearch(*22*) (**Fig. S11**).

Alignment of eight representative pathogens confirmed absolute conservation of all M1/M2 residues (**Fig. S12**), suggesting that Zn^{2+}-triggered ZSD dimerization is a common mechanism for controlling zinc uptake across these pathogenic bacteria.

ZnuBC activation

Because Zn^{2+} binding stabilizes the ZnuC zinc-sensing domain (ZSD) dimer, we hypothesized that Zn^{2+} removal would destabilize it. To test this, we treated ZnuBC with EDTA to strip Zn^{2+} and solved its cryo-EM structure (**Figs. S4d, S5d**). The EDTA-treated map lacked density for most of the ZSD and its Zn^{2+} ions (**Fig. 4b**). Alignment with the apo structure revealed broken two-fold symmetry: ZnuC subunits rotated by 6° and 3° relative to their ZnuB partners, reducing the ZnuC–ZnuC interface from 1,606 $Å^2$ to 86 $Å^2$, while ZnuB remained largely unchanged (RMSD 0.660 Å) (**Fig. 4c**). These data indicate that Zn^{2+} depletion unfolds the ZSD and increases ZnuC flexibility by disrupting its dimer interface.

Next, we asked whether nucleotide binding could induce conformational changes in this destabilized state. We added AMP-PNP to the EDTA-treated complex and solved its cryo-EM structure (**Figs. S4e, S5e**). Despite particle heterogeneity, heterogeneous and nonalignment classifications (**Fig. S13**) revealed a subset with distinct rearrangements (**Fig. 4d, S14**): the six ZnuB transmembrane helices showed varied periplasmic rotations, and periplasmic loops, including the α1 plug, became disordered (**Fig. S14**). ZSD densities remained heterogeneous and disordered, but the remainder of ZnuC shifted toward the membrane, with extra density attributable to AMP-PNP. The ZnuB–ZnuC interface expanded laterally and contracted vertically, disordering the α2 coupling helix. Thus, transporter activation appears to require Zn^{2+} removal, which destabilizes the ZSD dimer, followed by ATP binding, which drives ZnuC conformational changes that push on the α2 helices, twist the TM bundle, and open the periplasmic gate.

Alternating access transport model

To gain insights into potential mechanisms of Zn^{2+} transport by ZnuBC, we analyzed the collective dynamics of the cryoEM structures using the anisotropic network model (ANM) (*23, 24*). In general, molecular dynamics (MD) simulations are performed to investigate protein dynamics at the full atomic scale. However, MD simulations suffer from incomplete sampling of the conformational space, and the simulated events are usually confined to relatively more localized interactions that take place within microseconds. This is especially true for multimeric proteins in the presence of explicit water molecules and lipid bilayers. Here, we determined the global conformational changes in the structure of ZnuBC by performing an ANM-based normal mode analysis (*23-25*), using the *ProDy* interface (*26*). Normal mode analysis presents the advantage of yielding a spectrum of motions and extracting the most cooperative ones at the lowest frequency end of the spectrum.

We computed the intrinsic dynamics of ZnuBC by normal-mode analysis on both the apo and EDTA-treated structures, first in isolation and then embedded in an explicit lipid bilayer using the membrANM extension (*27*). The four lowest-frequency modes (ANM1–4) are illustrated in Fig. S16a–d and animated in Movies S1–S4. All four reflect motions dictated by the transporter's overall architecture and remain essentially unchanged by the membrane (**Fig. S15e**). Specifically, ANM1 is a global twisting of the ZnuB and ZnuC dimers, ANM2 is a bending of ZnuB relative to ZnuC, ANM3 is a tilting motion, and ANM4 corresponds to alternating opening toward the periplasm or cytosol. When we compare the mode spectra of the apo versus EDTA-

treated forms (**Fig. S15f**), ANM1, ANM2, and ANM4 retain their shapes with cosine-similarity >0.80, indicating that these key dynamic modes persist despite Zn^{2+}-induced structural changes.

Of interest is ANM mode 4, which predicts that the ZnuBC complex is capable of undergoing large-scale conformational changes that successively allow for Zn^{2+} access from the periplasm and Zn^{2+} release to the cytosol, consistent with an alternating access model (*28*). As can be seen in **Movie S4**, the opening to the periplasm is enabled by sampling a conformer that closely resembles the cryo-EM resolved outward-facing state (**Fig. 4e**); whereas the alternative conformer sampled in this cooperative mode represents an inward-facing state, yet to be resolved by experiments.

Exposure of the hydrophobic intramembrane cavity, lined by TM2 and TM4 of the ZnuB homodimer, to the periplasm coincides with narrowing of its cytoplasmic face, and the reverse occurs in the inward-facing state. Inward opening of the cytoplasmic end is coupled to a rotation of the α2 coupling helix and a rearrangement of the ZnuC dimer, which together occlude the periplasmic vestibule, expand the cytoplasmic interface between ZnuB and ZnuC, and likely facilitate Zn^{2+} release into the cytosol (**Fig. 4f; Movie S4**). These coordinated transitions support an alternating-access transport cycle for ZnuABC and explain the conformational heterogeneity seen in the EDTA/AMP-PNP dataset. However, neither the ANM predictions nor the current cryo-EM maps clarify whether the α1 plug that seals the intramembrane cavity becomes disordered or shifts during this cycle—a localized motion that would correspond to a higher-frequency mode beyond the lowest-frequency global rearrangements described here.

Discussion

Excess Zn^{2+} is toxic, so its uptake and intracellular levels must be tightly controlled. Based on our cryo-EM structures and functional assays, we propose the following transport cycle for ZnuABC (**Fig. 5**). Under Zn^{2+}-replete conditions, each ZnuC zinc-sensing domain (ZSD) binds Zn^{2+}, dimerizes, and locks ZnuB in an outward-facing, closed conformation that is refractory to ATP (**Fig. 5a**). When cellular Zn^{2+} is depleted by enzymes or transcription factors, Zn^{2+} dissociates from the ZSDs, destabilizing their dimer interface and disordering the ZnuC NBDs while ZnuB remains outward-facing and sealed (**Fig. 5b**). ATP binding then induces a conformational change, likely transmitted via the Q-loop of ZnuC and the α2 helices of ZnuB, that disrupts the α1 plug and opens the periplasmic vestibule (**Fig. 5c**). The periplasmic chaperone ZnuA docks, delivers Zn^{2+} into the hydrophilic cavity lined by Asp36 and His40 (**Fig. 2e**), and is released as ZnuB transitions to an occluded state (**Fig. 5d–e**). Finally, ATP hydrolysis in ZnuC drives the switch to an inward-facing state (via ANM mode 4; **Fig. 4f**), releasing Zn^{2+} into the cytosol and resetting the ZSD sensor for the next cycle (**Fig. 5b**) or re-locking the transporter when Zn^{2+} is sufficient (**Fig. 5a**).

Normal-mode analysis with the anisotropic network model (ANM) predicts that ZnuBC can access an inward-facing state through intrinsic, low-frequency motions consistent with an alternating-access cycle. ANM efficiently captures these cooperative, near-equilibrium transitions, although it cannot overcome large energy barriers; using a coarse-grained ANM smooths the landscape to sample relevant substates at the cost of atomic detail. As shown by Tirion (*29*), these global modes depend mainly on network connectivity. To validate our inward-facing model (**Fig. 4f; Movie S4**), we compared it to the only experimental inward-facing type II ABC transporter (HI1470/1 from Haemophilus influenzae, PDB 2NQ2) (*30*). Superimposition gives an RMSD of 3.92 Å over 753 Cα atoms, and both structures show the NBDs moving apart

and the NBD–TMD interface expanding (**Fig. S16**). Still, additional structures in inward-facing, ZnuA-bound, and occluded states are needed to fully define the ZnuABC transport cycle.

ZnuABC expression is controlled by the Zur transcription factor, but its post-translational regulation is unknown. We discovered a Zn^{2+} sensor in the C-terminal zinc-sensing domain (ZSD) of ZnuC, defined by the conserved motif CxxxHxCCxGxP and a histidine-rich tail. This motif creates two high-affinity Zn^{2+} sites (M1 and M2) that prevent toxic Zn^{2+} overaccumulation and support cell growth (**Fig. 4b**). Based on the classification of ABC transporters (*31*), ZnuABC belongs to type II ABC transporters. Five other type II ABC transporter structures have been reported: ButCD-F (PDB code 2QI9), HI1470/1 (PDB code 2NQ2), FhuCDB (PDB code 7LB8), BhuUV (PDB code 5B57), and PsaBC (PDB code 7KYP). We performed structural alignments of the ZnuC ZSD with the NBD C-termini of five type II ABC importers (PsaC, ButD, HI1470, FhuD, and BhuV), as shown in **Fig. S17**. Unlike the ZnuC ZSD, which comprises two short α-helices (α6–7), a β-strand (β13), and a long loop, the C-termini of the compared NBDs consist of either a single long helix (PsaC) or a long helix followed by two β-strands (ButD, HI1470, FhuD, and BhuV). These differences highlight the unique structural features of the ZnuC ZSD.

Beyond the Zn^{2+} ABC transporters, we previously proposed that bacterial ZIP-family Zn^{2+} transporter *Bb*ZIP has a histidine-rich loop between TM3 and TM4 and functions as an intracellular Zn^{2+} sensor to regulate the transporter activity (*32*). In plants, a histidine-rich loop in Arabidopsis IRT1, also a ZIP member, senses metals and triggers endosomal sorting and vacuolar degradation of IRT1 (*33*). A histidine-rich cluster in human ZIP4 mediates its ubiquitination and degradation to prevent Zn^{2+} toxicity (*34*). It appears that all living organisms have evolved versatile ways to regulate the activity of Zn^{2+} transporters post-translationally through inhibition or degradation to prevent excess accumulation of Zn^{2+} and toxicity. Further studies are needed to see if this regulation exists in other essential but toxic metal micronutrients.

Zn^{2+} ABC transporters are bacterium-specific and exist in most high-risk pathogens (**Fig. S11**). The structures of the Zn^{2+} ABC transporter ZnuBC provide a basis for the development of antibiotics and vaccines targeting the conserved sites, such as the α1 plug to seal the intramembrane cavity in ZnuB. The conserved Zn^{2+} transport cavity is another possible target. The cavity is elongated and larger than accommodating a single Zn^{2+}. A potential inhibitor blocking the cavity may help reduce pathogenicity by preventing the evasion of pathogens from the hosts' nutritional immunity.

References and Notes

1. S. Clemens, The cell biology of zinc. *J Exp. Bot.* **73**, 1688-1698 (2022).
2. J. Hu, Toward unzipping the ZIP metal transporters: structure, evolution, and implications on drug discovery against cancer. *FEBS J.* **288**, 5805-5825 (2021).
3. C. Stanton, D. Sanders, U. Kramer, D. Podar, Zinc in plants: Integrating homeostasis and biofortification. *Mol. Plant* **15**, 65-85 (2022).
4. D. K. Blencowe, A. P. Morby, Zn(II) metabolism in prokaryotes. *FEMS Microbiol. Rev.* **27**, 291-311 (2003).
5. T. Kambe, K. M. Taylor, D. Fu, Zinc transporters and their functional integration in mammalian cells. *J. Biol. Chem.* **296**, 100320 (2021).
6. S. I. Patzer, K. Hantke, The ZnuABC high-affinity zinc uptake system and its regulator Zur in Escherichia coli. *Mol. Microbiol.* **28**, 1199-1210 (1998).

7. C. C. Murdoch, E. P. Skaar, Nutritional immunity: the battle for nutrient metals at the host–pathogen interface. *Nat. Rev. Microbiol.* **20**, 657-670 (2022).
8. J. Wątły, S. Potocki, M. Rowińska-Żyrek, Zinc Homeostasis at the Bacteria/Host Interface—From Coordination Chemistry to Nutritional Immunity. *Chemistry – A European Journal* **22**, 15992-16010 (2016).
9. E. A. Maunders *et al.*, Zinc acquisition and its contribution to Klebsiella pneumoniae virulence. *Front Cell Infect Mi* **13**, (2024).
10. J. Wang, L. Xiu, Y. Qiao, Y. Zhang, Virulence regulation of Zn2+ uptake system znuABC on mesophilic Aeromonas salmonicida SRW-OG1. *Frontiers in Veterinary Science* **10**, (2023).
11. R. E. R. S. Santos *et al.*, The Zinc Transporter ZnuABC Is Critical for the Virulence of Chromobacterium violaceum and Contributes to Diverse Zinc-Dependent Physiological Processes. *Infect. Immun.* **89**, (2021).
12. K. J. Tanaka, S. Song, K. Mason, H. W. Pinkett, Selective substrate uptake: The role of ATP-binding cassette (ABC) importers in pathogenesis. *Biochim. Biophys. Acta Biomembr.* **1860**, 868-877 (2018).
13. K. P. Grim *et al.*, The Metallophore Staphylopine Enables Staphylococcus aureus To Compete with the Host for Zinc and Overcome Nutritional Immunity. *mBio* **8**, 10.1128/mbio.01281-01217 (2017).
14. M. D'Orazio *et al.*, The capability of Pseudomonas aeruginosa to recruit zinc under conditions of limited metal availability is affected by inactivation of the ZnuABC transporter†. *Metallomics* **7**, 1023-1035 (2015).
15. L. Bayle *et al.*, Zinc uptake by Streptococcus pneumoniae depends on both AdcA and AdcAII and is essential for normal bacterial morphology and virulence. *Mol. Microbiol.* **82**, 904-916 (2011).
16. S. Campoy *et al.*, Role of the High-Affinity Zinc Uptake znuABC System in Salmonella enterica Serovar Typhimurium Virulence. *Infect. Immun.* **70**, 4721-4725 (2002).
17. J. M. Moore, E. L. Bell, R. O. Hughes, A. S. Garfield, ABC transporters: human disease and pharmacotherapeutic potential. *Trends in Molecular Medicine* **29**, 152-172 (2023).
18. C. Thomas, R. Tampé, Structural and Mechanistic Principles of ABC Transporters. *Annual Review of Biochemistry* **89**, 605-636 (2020).
19. K. Hantke, Bacterial zinc uptake and regulators. *Current Opinion in Microbiology* **8**, 196-202 (2005).
20. E. Krissinel, K. Henrick, Inference of macromolecular assemblies from crystalline state. *J Mol Biol* **372**, 774-797 (2007).
21. K. J. Linton, Structure and function of ABC transporters. *Physiology (Bethesda)* **22**, 122-130 (2007).
22. L. Zimmermann *et al.*, A Completely Reimplemented MPI Bioinformatics Toolkit with a New HHpred Server at its Core. *J Mol Biol* **430**, 2237-2243 (2018).
23. A. R. Atilgan *et al.*, Anisotropy of fluctuation dynamics of proteins with an elastic network model. *Biophys J* **80**, 505-515 (2001).
24. I. Bahar, T. R. Lezon, A. Bakan, I. H. Shrivastava, Normal mode analysis of biomolecular structures: functional mechanisms of membrane proteins. *Chem Rev* **110**, 1463-1497 (2010).
25. T. Haliloglu, I. Bahar, B. Erman, Gaussian dynamics of folded proteins. *Physical review letters* **79**, 3090 (1997).
26. S. Zhang *et al.*, ProDy 2.0: increased scale and scope after 10 years of protein dynamics modelling with Python. *Bioinformatics* **37**, 3657-3659 (2021).

27. Y. Zhang, S. Zhang, J. Xing, I. Bahar, Normal mode analysis of membrane protein dynamics using the vibrational subsystem analysis. *J Chem Phys* **154**, 195102 (2021).
28. M. L. Oldham, A. L. Davidson, J. Chen, Structural insights into ABC transporter mechanism. *Curr. Opin. Struc. Biol.* **18**, 726-733 (2008).
29. M. M. Tirion, Large amplitude elastic motions in proteins from a single-parameter, atomic analysis. *Physical review letters* **77**, 1905 (1996).
30. H. W. Pinkett, A. T. Lee, P. Lum, K. P. Locher, D. C. Rees, An Inward-Facing Conformation of a Putative Metal-Chelate-Type ABC Transporter. *Science* **315**, 373-377 (2007).
31. C. Thomas *et al.*, Structural and functional diversity calls for a new classification of ABC transporters. *FEBS Lett* **594**, 3767-3775 (2020).
32. C. Pang, J. Chai, P. Zhu, J. Shanklin, Q. Liu, Structural mechanism of intracellular autoregulation of zinc uptake in ZIP transporters. *Nature Communications* **14**, 3404 (2023).
33. G. Dubeaux, J. Neveu, E. Zelazny, G. Vert, Metal sensing by the IRT1 transporter-receptor orchestrates Its own degradation and plant metal nutrition. *Mol. Cell* **69**, 953-964 e955 (2018).
34. X. Q. Mao, B. E. Kim, F. D. Wang, D. J. Eide, M. J. Petris, A histidine-rich cluster mediates the ubiquitination and degradation of the human zinc transporter, hZIP4, and protects against zinc cytotoxicity. *J. Biol. Chem.* **282**, 6992-7000 (2007).
35. S. Q. Zheng *et al.*, MotionCor2: anisotropic correction of beam-induced motion for improved cryo-electron microscopy. *Nat. Methods* **14**, 331-332 (2017).
36. K. Zhang, Gctf: Real-time CTF determination and correction. *J. Struct. Biol.* **193**, 1-12 (2016).
37. J. Zivanov *et al.*, New tools for automated high-resolution cryo-EM structure determination in RELION-3. *Elife* **7**, e42166 (2018).
38. A. Punjani, H. Zhang, D. J. Fleet, Non-uniform refinement: adaptive regularization improves single-particle cryo-EM reconstruction. *Nat. Methods* **17**, 1214-1221 (2020).
39. D. M. McSweeney, S. M. McSweeney, Q. Liu, A self-supervised workflow for particle picking in cryo-EM. *IUCrJ* **7**, 719-727 (2020).
40. E. F. Pettersen *et al.*, UCSF chimera - A visualization system for exploratory research and analysis. *J. Comput. Chem.* **25**, 1605-1612 (2004).
41. J. Vilas *et al.*, Local resolution estimates of cryoEM reconstructions. *Curr. Opin. Struc. Biol.* **64**, 74-78 (2020).
42. X. Dai, L. Wu, S. Yoo, Q. Liu, Integrating AlphaFold and deep learning for atomistic interpretation of cryo-EM maps. *Brief Bioinform* **24**, 2023.2002. 2002.526877 (2023).
43. A. Casañal, B. Lohkamp, P. Emsley, Current developments in Coot for macromolecular model building of electron cryo-microscopy and crystallographic data. *Protein Sci.* **29**, 1055-1064 (2020).
44. P. D. Adams *et al.*, PHENIX: a comprehensive Python-based system for macromolecular structure solution. *Acta crystallogr. D* **66**, 213-221 (2010).
45. C. J. Williams *et al.*, MolProbity: More and better reference data for improved all-atom structure validation. *Protein Sci.* **27**, 293-315 (2018).
46. E. Eyal, G. Lum, I. Bahar, The anisotropic network model web server at 2015 (ANM 2.0). *Bioinformatics* **31**, 1487-1489 (2015).
47. E. Eyal, L. W. Yang, I. Bahar, Anisotropic network model: systematic evaluation and a new web interface. *Bioinformatics* **22**, 2619-2627 (2006).

48. A. L. Lomize, S. C. Todd, I. D. Pogozheva, Spatial arrangement of proteins in planar and curved membranes by PPM 3.0. *Protein Sci.* **31**, 209-220 (2022).
49. K. Tamura, G. Stecher, S. Kumar, MEGA11 molecular evolutionary genetics analysis version 11. *Mol. Biol. Evol.* **38**, 3022-3027 (2021).

Acknowledgments: We thank the LBMS staff for their help with the cryo-EM operation and data acquisition. The work used the Laboratory for Biomolecular Structure (LBMS) which is supported by the U.S. Department of Energy, Office of Science, Office of Biological and Environmental Research.

Funding:

U.S. Department of Energy (DOE), Office of Biological and Environmental Research KP1601011 (QL)

National Institutes of Health grant NIH R01GM139297 (IB)

Author contributions: Q.L. designed the study and experiments. P.C., Q.Z., H.N., and Q.L. performed the experiments. P.C., I.B., and Q. L. analyzed the data. Q.L. and I.B. wrote the manuscript with help from other coauthors.

Competing interests: Authors declare that they have no competing interests.

Data and materials availability: The 3-dimentional cryo-EM density map has been deposited in the Electron Microscopy Data Bank under the accession number EMD-70570 for AMP-PNP state [https://www.emdataresource.org/EMD-70570], EMD-70571 for ATP state [https://www.emdataresource.org/EMD-70571], EMD-70572 for apo state [https://www.emdataresource.org/EMD-70572], EMD-70573 for EDTA-treated zinc free state [https://www.emdataresource.org/EMD-70573]. Atomic coordinates have been deposited in the Protein Data Bank under the accession numbers 9OKO for AMP-PNP state [https://doi.org/10.2210/pdb9oko/pdb], 9OKP for ATP state [https://doi.org/10.2210/pdb9okp/pdb], 9OKQ for apo state [https://doi.org/10.2210/pdb9okq/pdb], and 9OKR for EDTA-treated, zinc-free state [https://doi.org/10.2210/pdb9okr/pdb].Supplementary Materials

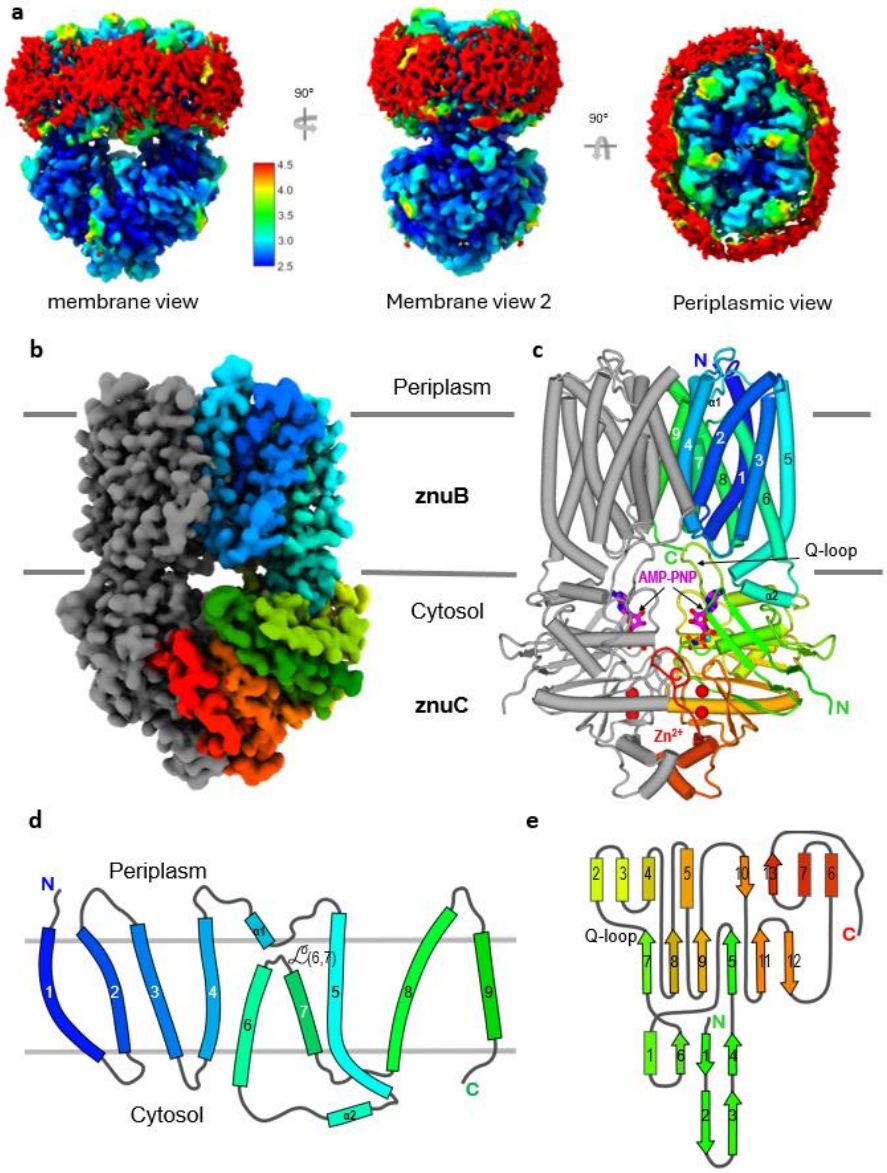

Fig. 1. Overall structure of the ZnuB-ZnuC transporter. **a**, Three views of the reconstructed map with surface colored by local resolutions. Amphipol A8-35 densities are mostly disordered and are colored red. **b**, CryoEM density map of the ZnuBC subunits of ZnuABC transporter. One subunit is colored rainbow and the other, gray. **c**, Overall structure of the ZnuBC dimer. The coloring is as in panel a. Four-bound Zn2+ ions are shown as red spheres. Two AMP-PNP molecules are shown as magenta sticks. **d**, Topology diagram of a ZnuB subunit. **e**, Topology diagram of a ZnuC subunit.

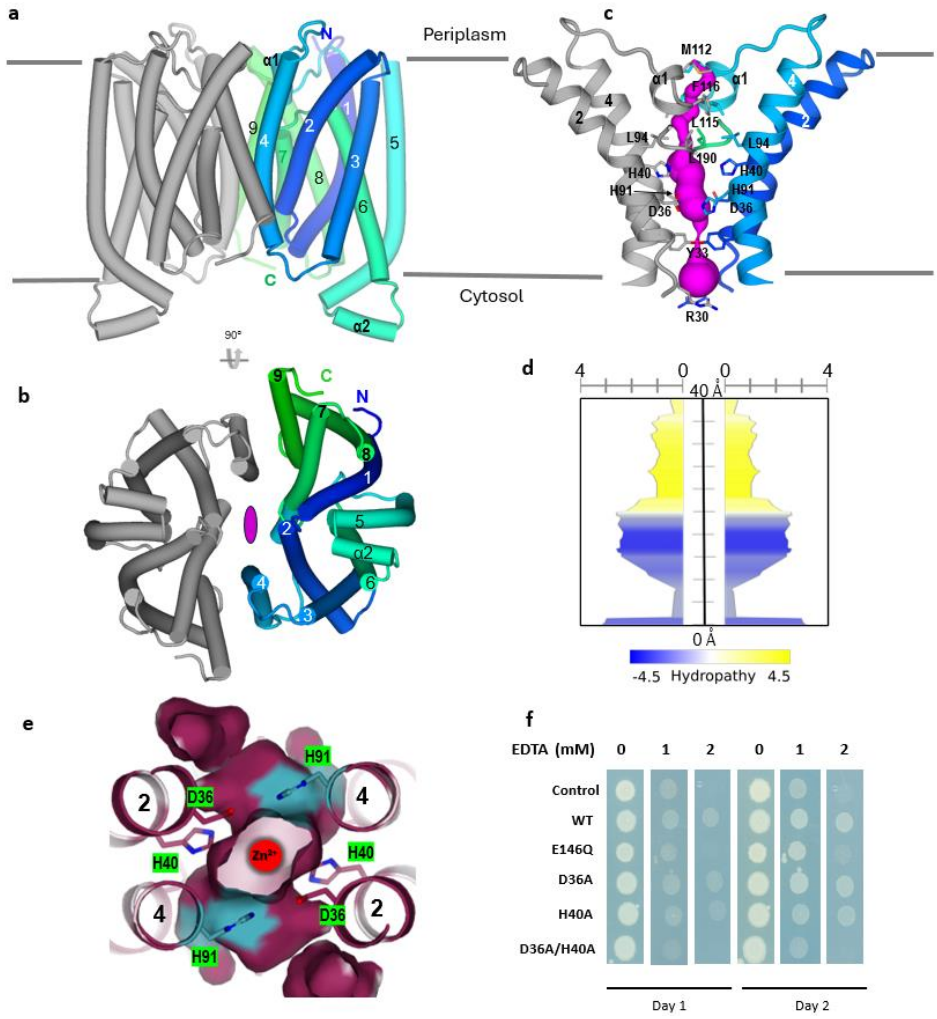

Fig. 2. Structure of ZnuB dimer. a-b, Two views of the overall structure of the dimer, viewed from the side and the cytosol, respectively. The dimer has a twofold symmetry. **c**, The membrane transport channel (*magenta surface*) lined by the labeled TM2 and TM4 residues from each monomer. **d**, Quantification of the size and hydrophobicity of the transport channel. **e**, An elongated Zn^{2+}-binding cavity at the center of the transmembrane region. The surface color shows the conservation level: *magenta*, more conserved; *cyan*, relatively less conserved. **f**, Functional characterization of zinc uptake and cell viability by removing Zn^{2+} using EDTA.

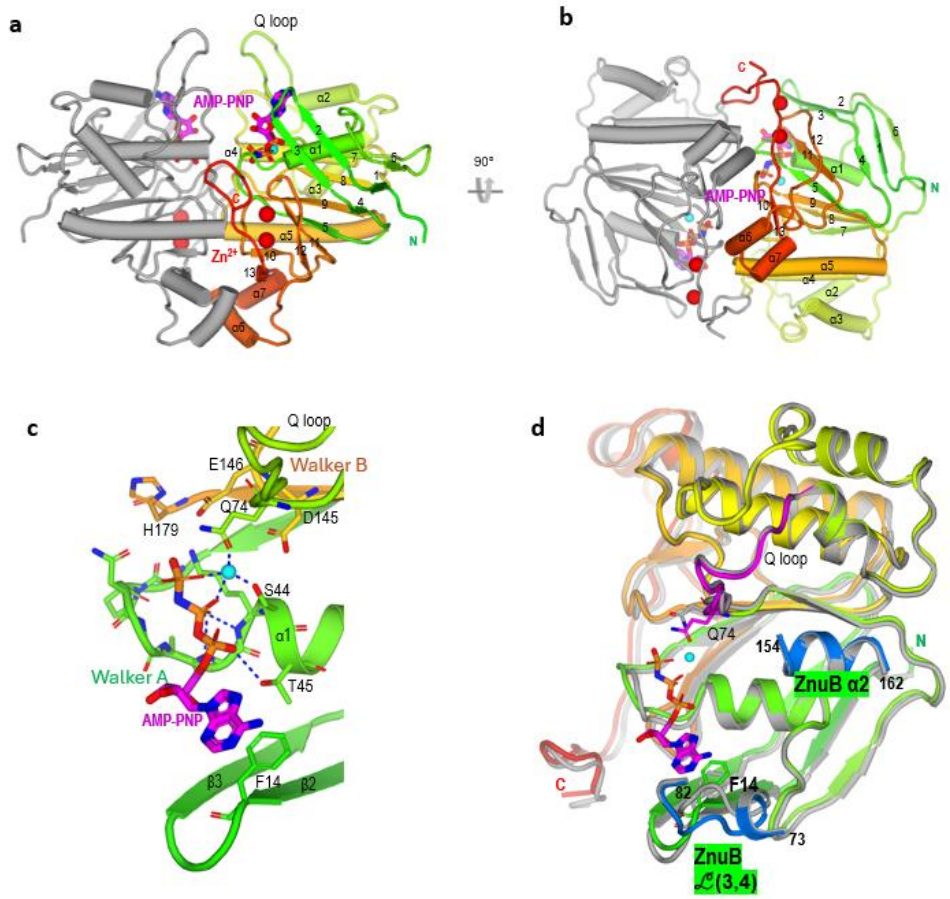

Fig. 3. Structure of the ATP-binding cassette subunit ZnuC and its interaction with ZnuB. a-b, Side (**a**) and bottom (**b**) views of the AMP-PNP-bound structure of the ZnuC dimer. The coloring is the same as **Fig. 1c**. **c**, Interactions between AMP-PNP and the NBD of ZnuC. The *cyan sphere* is an Mg^{2+} ion, coordinated by S44, Q74, and AMP-PNP. **d**, Superimposition of the AMP-PNP-bound and apo structures. The apo-form structure is colored gray. The ZnuB loop L(3,4) and α2 coupling helix are indicated.

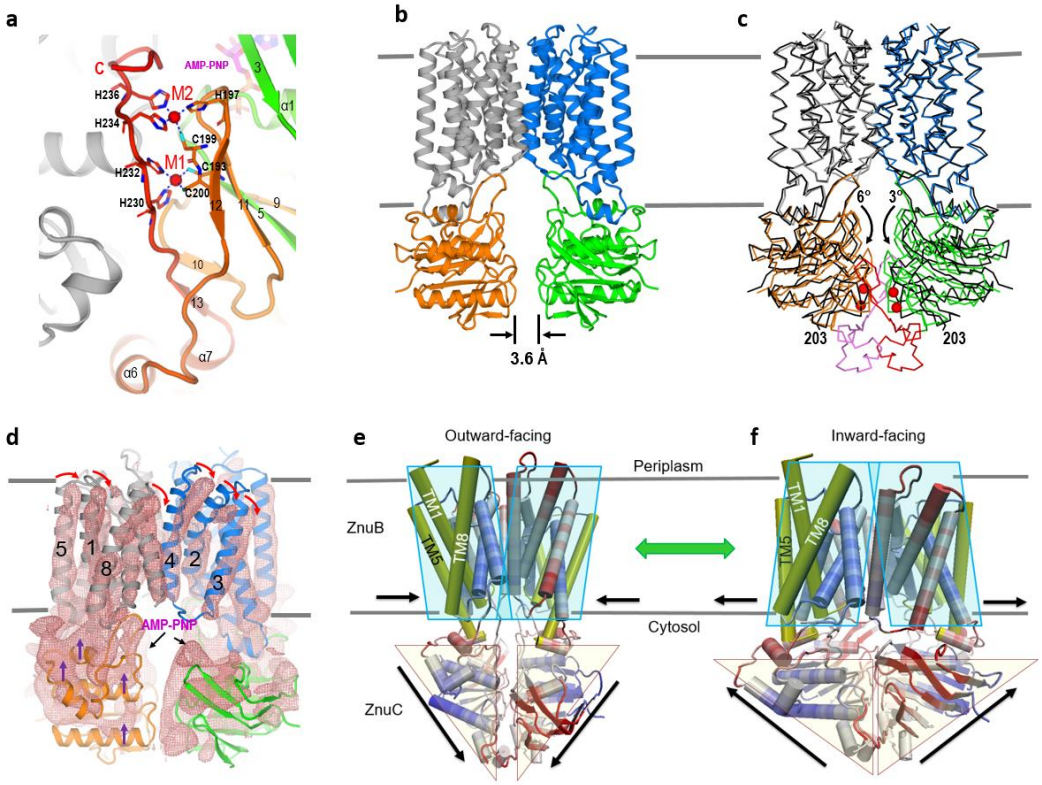

Fig. 4. Intracellular zinc-sensing and transport cycle regulation by ZnuC ZSD. **a**, Zn^{2+} binding sites M1 and M2 at the ZnuC ZSD. **b**, CryoEM structure of EDTA-treated Zn^{2+}-free state. Compared to the apo structure, the two ZnuC monomers moved away from each other by 3.6 Å. **c**, Superimposed apo and ETDA-treated structures to show conformational changes associated with Zn^{2+} sensing and regulation. Arrows show rotations of ZnuC relative to respective interacting ZnuB. **d**, CryoEM map for the EDTA- and AMP-PNP-treated state. The EDTA-treated structure was manually aligned with the map. Red curved arrows indicate rotations, and purple straight arrows represent translations. Black arrows indicate possible densities for AMP-PNP. **e**-**f**, Anisotropic network model (ANM) analysis predicts an alternating access mechanism for ZnuBC, where ZnuC moves toward ZnuB, and ZnuB changes its conformation from outward-facing (**e**) to inward-facing (**f**) to enable Zn^{2+} transport (**Fig. S14 and Movie S4**).

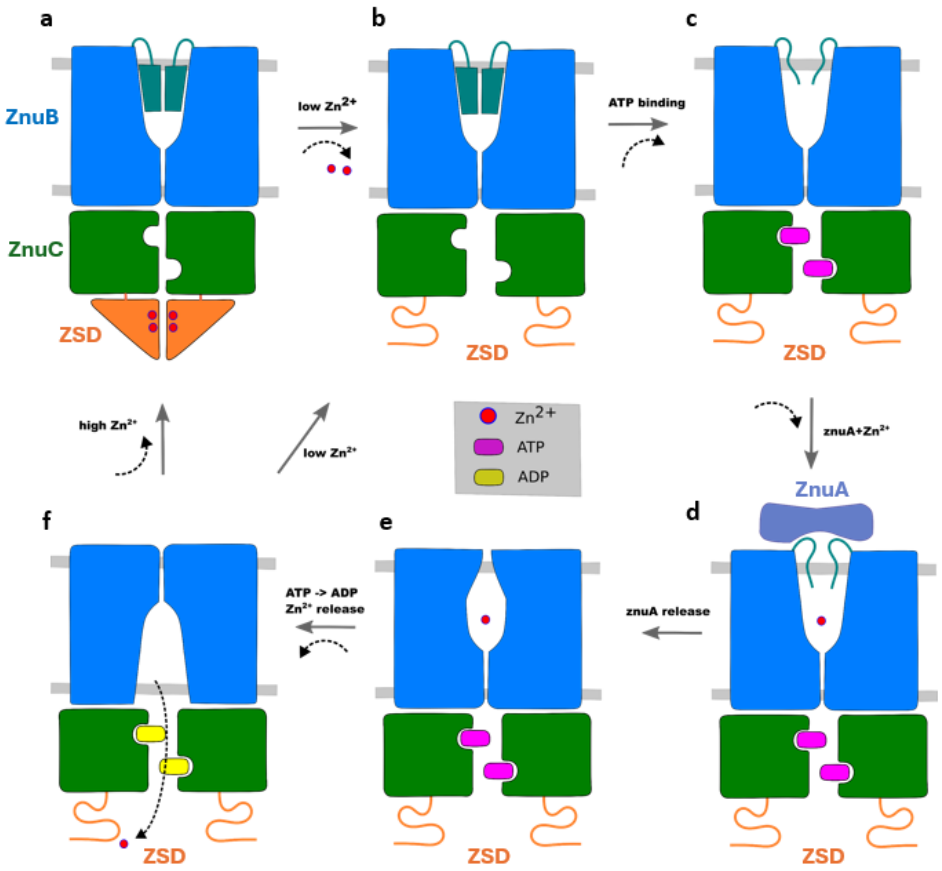

Fig. 5. Proposed zinc uptake and regulation mechanism. a, ZSD binds intracellular Zn^{2+} and dimerization in a nucleotide-independent manner. The transporter is in an outward-facing inhibited state by two seal plugs. **b**, Under extremely low Zn^{2+} conditions, ZSD loses Zn^{2+} and becomes disordered. The two ZnuC monomers separate from each other. The transporter remains sealed. **c**, ATP-binding to ZnuC NBD activates the transporter by disordering the sealing plug. **d**, In the presence of extracellular Zn^{2+}, ZnuA binds and delivers Zn^{2+} to the intramembrane Zn^{2+}-binding cavity. The transporter is in an outward-facing, open state. **e**, Binding of Zn^{2+} to the pore triggers an occluded state and release of ZnuA. **f**, ATP hydrolysis drives the conformational changes to an inward-facing state. Zn^{2+} is released from the cytoplasmic side. ZSD will monitor intracellular Zn^{2+} content to determine the execution of another transport cycle (**b**) or inhibition (**a**). Of the six models, models a-c have experimental support and d-f are hypothetical and speculative.

Materials and Methods

ZnuA-ZnuB-ZnuC cloning

The *E.coli* gene *ZnuCB* was amplified from genomic DNA (strain DH5α) using the forward primer 5′-GCCAGGATCCGAATTCACAAGTCTGGTTTCCCTGGA-3′ and the reverse primer 5′-GGCGAAGCTTTTAGCTGGCCTGCTTTTTCA-3′, which introduced unique BamHI and HindIII restriction sites flaking the *ZnuCB* gene. The *E. coli ZnuA* was amplified from genomic DNA (strain DH5α) using the forward primer 5′-TATACATATGTTACATAAAAAAACGCTTCT -3′ and the reverse primer 5′-CAGACTCGAGATCTCCTTTCAGGCAGCTCG -3′, which introduced unique NdeI and XhoI restriction sites flaking the ZnuA gene. The PCR products were inserted into pGEM-T-Easy vector according to the manufacturer's instructions. The sequences were confirmed by DNA sequencing with the sequencing primers M13F 5′-GTAAAACGACGGCCAGTG-3' and M13R 5'-GGAAACAGCTATGACCATG-3'. The *ZnuCB* was digested with BamHI and HindIII and ligated into the pET-Duet1 vector. Then *ZnuA* was digested with NdeI and XhoI and ligated into the pET-Duet1-ZnuCB. The sequence was confirmed by DNA sequencing with the sequencing. All primers used are listed in **Table S2**. The assembled plasmid pET-Duet1_ZnuA-ZnuCB was then transformed into *E. coli* C43 (DE3) cells.

ZnuB-ZnuC expression and purification

The cells transformed with pET-Duet1_ZnuA-ZnuCB were cultured at 37°C to the density at OD_{600} of 0.8-1.2 in Terrific Broth (TB) medium supplemented with 100 µg/ml carbenicillin. Protein production was induced with 0.5 mM isopropyl-β-D-thiogalactopyranoside (IPTG). Cells were harvested 4 hrs after the IPTG induction by centrifugation at 6000xg for 15 min. Cells were resuspended in cold lysate buffer (20 mM HEPES, pH 7.4, 200 mM NaCl, and 20% glycerol) containing 0.1 mM phenylmethysulfonyl fluoride (PMSF). The cells were lysed by passage through an EmlsiFlex-C3 homogenizer (Avestin, Ottawa, Canada) six times at 15,000 psi. Cell debris was removed by centrifugation 31,360xg for 1 hr. The supernatant was collected, and the membrane was harvested by centrifugation at 223,608xg for 2 hrs. The membrane pellet was resuspended in resuspend buffer (20 mM HEPES, pH 7.4, 200 mM NaCl, 20% glycerol, and 10 mM imidazole) supplemented with protease inhibitor cocktail EDTA free (abcam, Waltham, MA, Cat# ab270055). The membrane was solubilized with 1.5% n-Dodecyl-B-D-Maltoside (DDM) supplemented with 50 µM $ZnCl_2$ for 2 hrs. The insoluble components were removed by centrifugation at 113,210xg for 1 hr. The supernatant was applied to a pre-equilibrated Ni^{2+}-NTA column (Anatrace, Maumee, OH, Cat# SUPER-NINTA100). The column was washed by 10 column volumes (cv) of wash buffer (20 mM HEPES, pH 7.4, 200 mM NaCl, 20% glycerol, 40 mM imidazole, and 0.05% DDM). The protein was eluted by elute buffer (20 mM HEPES, pH 7.4, 200 mM NaCl, 200 mM imidazole, and 0.05% DDM) and concentrated to 5 mg/ml by using a 100 kDa molecular-weight cutoff concentrator (Millipore Sigma, Burlington, MA, USA). The purified complex contained ZnuBC (**Fig. S1**).

Amphipol reconstitution of ZnuB-ZnuC complex

The concentrated protein (5mg/ml) was mixed with amphipol A8-35 (Anatrace, Maumee, OH, Cat# A8-35) in a mass ratio of protein/amphipol of 1:5 (w/w). The mixture was incubated at 4°C for 20 hrs. Then, SM-2 Bio-Beads (Bio-Rad, Cat#1523920) were added at a mass ratio of protein/beads of 1:100 (w/w) ratio to the mixture. The mixture was incubated at 4°C for 3 hrs. Prior to use, Bio-Beads were soaked with buffer containing 20 mM HEPES, pH 7.4, and 200 mM NaCl overnight at 4°C. The Bio-Beads were removed by passing through a micro Bio-Spin

chromatography column. The flow-through containing the reconstitution mixture was centrifugated at 20,000xg for 1 hr at 4°C. The supernatant was applied to a Superdex 200 Increase column (GE Healthcare, Inc., Chicago, IL, USA) and eluted in a buffer containing 20 HEPES, pH 7.4 and 100 mM NaCl. The fractions containing the ZnuBC complex were collected and concentrated to 2 mg/ml for cryo-electron microscopy analysis. To prepare the EDTA-treated ZnuBC sample, the amphiphilic-reconstituted ZnuBC sample was incubated with 0.5 mM EDTA for 2 hr on ice before loading to the pre-equilibrated Superdex 200 column.

ATPases Activity Assay

ATPase activity assay was performed using ATPase/GTPase Activity Assay Kit (Sigma-Aldrich., Catalog No. MAK113) according to the manufacturer's protocol. Three replicates were measured for each sample. Buffer (20 mM HEPES, pH 7.4, 100 mM NaCl) without protein was tested as the control. The wild type and E146Q mutant reconstituted into A8-35 were used for the assay. The concentration of each sample was 0.2 mg/ml, and 10 µl was used for each replicate. Reactions were incubated at room temperature for 30 minutes before Reagent was added to terminate the reactions. After 30min incubation for colorimetric product generation, absorbance at 620 nm was measured at room temperature using a TECAN's Spark 20M multimode reader (Tecan Trading AG, Switzerland). ATPase activity was calculated as phosphate (µM) produced by 1 mg protein per minute under experimental conditions.

Bacterial growth viability assay

The mutation expression constructs were created with Q5 Site-Directed Mutagenesis Kit (New England BioLabs, Inc., Ipswich, MA) according to the manufacturer's instructions. The primers used are listed in **Table S1**. The empty pETDuet-1 vector was used for vector control.

The expression constructs were transformed into *E. coli* C43 (DE3) competent cells. Three colonies were inoculated into 5 mL of LB media at 37°C for overnight culture. 100 µl culture was used to inoculate 5 ml fresh LB media. When the OD_{600} value reached between 0.8-1.0, 1 mM IPTG (final) was added to induce the expression at 37 °C for 2 hours. Cells were then diluted to OD_{600} of 0.1, 0.01, 0.001, 0.0001, 0.00001, and 0.000001 with dilution buffer (20 mM HEPES, pH 7.4, 135 mM NaCl, and 5 mM KCl). Two microliters of diluted cells were placed on LB-Agar plates supplemented with 100 µg/ml carbenicillin, 1 mM IPTG, and various concentrations of ethylenediaminetetraacetic acid (EDTA, 0, 1, 2 , and 3 mM), ZnCl2 (0, 1, 2 mM), and their combinations. The plates were placed at 37 °C for bacterial growth. The plates were imaged every 24 hrs over three days.

Cryo-EM sample preparation and data collection

Three microliters of the reconstituted nanodiscs containing nucleotide-free ZnuBC were applied to a glow-discharged (15 mA current for 15 sec) 300-mesh R 0.6/1 UltrAuFoil Holey Gold grid (Electron Microscopy Sciences, Hatfield, PA, Cat# Q350AR1A). After waiting for about 60 sec, the grid was plunge-freezed to liquid ethane using a ThermoFisher Mark IV vitrobot (ThermoFisher Scientific, Waltham, MA) with a blotting condition of 3.5 sec blot time, 0 blot force, and 100% humidity at 6°C. For ATP and AMP-PNP samples, 5 mM ATP or AMP-PNP was briefly incubated with 10 mM Mg^{2+} and ZnuBC for 60 sec at room temperature before blotting with the same condition as the nucleotide-free samples.

Cryo-EM data for AMP-PNP state, ATP state, apo state, EDTA-treated state, and EDTA-treated AMP-PNP state were collected at the LBMS facility at Brookhaven National Laboratory using a ThermoFisher Titan Krios 300 kV electron microscope equipped with a Gatan K3 camera and a

BioQuantum energy filter. The physical pixel size used for all data collection is 0.666 Å. The beam size is 1.45 µm in diameter, covering the entire 0.6-µm hole. For each movie data frame, a total dose of 66 $e^-/Å^2$ was fractioned to 50 frames using the ThermoFisher data acquisition program EPU. All data sets were collected with an energy filter width of 15 eV which was centered every 1 hr of data acquisition. Data collection statistics are listed in **Table S2**.

Cryo-EM data processing

Fractioned movies were motion-corrected and averaged using MotionCorr2 (*35*) with a bin factor of 2. Averaged micrographs were further corrected by CTF estimation using Gctf (*36*). Micrographs with an estimated resolution better than 4.5 Å were selected for further use. Particles were initially picked in Relion3 (*37*) and cleaned up in cryoSPARC (*38*). Then the cleaned particles were used for training and particle picking using Kpicker (*39*).

For each data set, the picked particles were extracted at 256 pixels and binned to 64 pixels with a pixel size of 2.664 Å. We used cryoSPARC (*38*) for 2D class averaging to very generously select classes and particles 3D classification and refinement. With three classes each, selected particles were used for two cycles of *ab initio* reconstruction followed by 3D heterogenous refinements with a particle size of 64 pixels (2.664 Å) in cryoSPARC. The particles belonging to classes with structural features were centered and re-extracted at 256 pixels and binned to 128 pixels with a pixel size of 1.332 Å. The re-extracted particles were used for 3D heterogeneous refinement using 3 or 4 classes. The process is repeated in cryoSPARC until there is no improvement in the refined map resolution as estimated by the gold-standard Fourier Shell Correlation (GS-FSC). There was no symmetry used during the iterative *ab initio* model generation and 3D heterogenous refinements in cryoSPARC.

Particles from the best class or classes in cryoSPARC were auto-refined to convergence in Relion3 (*37*) followed by non-alignment 3D classification and local refinement without a symmetry (**Fig. S3**). Particles from the best 3D class or classes with the best structural feature as visualized in Chimera (*40*) were selected for non-uniform refinement and local refinement in cryoSPARC. With the AMP-PNP, ATP, and apo states, C2 symmetry was justified to be appropriate based on GS-FSC (**Fig. S4**). All final particles are 128 pixels except for the ANP-PNP data which we extracted the final particles at 160 pixels. Local resolutions were estimated using BlocRes (*41*). Data processing and reconstruction statistics are listed in **Table S2.**

Model building and refinement

To enhance the features for model building and visualization, the masked and filtered amps were processed by CryoFEM, which is a 3D convolutional neuron network (3D-CNN) model for local map sharpening and feature enhancement (*42*). The models were built in COOT (*43*) and refined real space using PHENIX (*44*). The refined models were validated using Molprobity (*45*). The refinement statistics are listed in **Table S2**.

Evaluation of transporter dynamics

All analyses for examining the dynamics of ZnuBC including its potential transition to inward-facing state were performed using the *ProDy* API(*26*). The Anisotropic Network Model (ANM) analysis (*46, 47*) on ZnuBC was conducted by constructing Hessian matrix ($3N \times 3N$) for the tetrameric apo structure (ZnuBC) and the EDTA treated structure (no ZSD) based on Cα coordinates. Explicit membrane ANM (ex MembrANM) (*27*), a method developed to incorporate lipid membrane in the ANM studies of membrane proteins embedded in an explicit membrane were also performed on the apo structure to assess the effect of membrane on protein dynamics.

The membrane was constructed using the OPM server (*48*). The Hessian matrices were decomposed into ANM normal modes to extract the lowest frequency (softest) modes which encapsulate global and cooperative motions. The first four ANM modes from the apo structure were reconstructed into 3D motions to visualize the individual mode motions (**Fig. S15 and Movies S1-S4**).

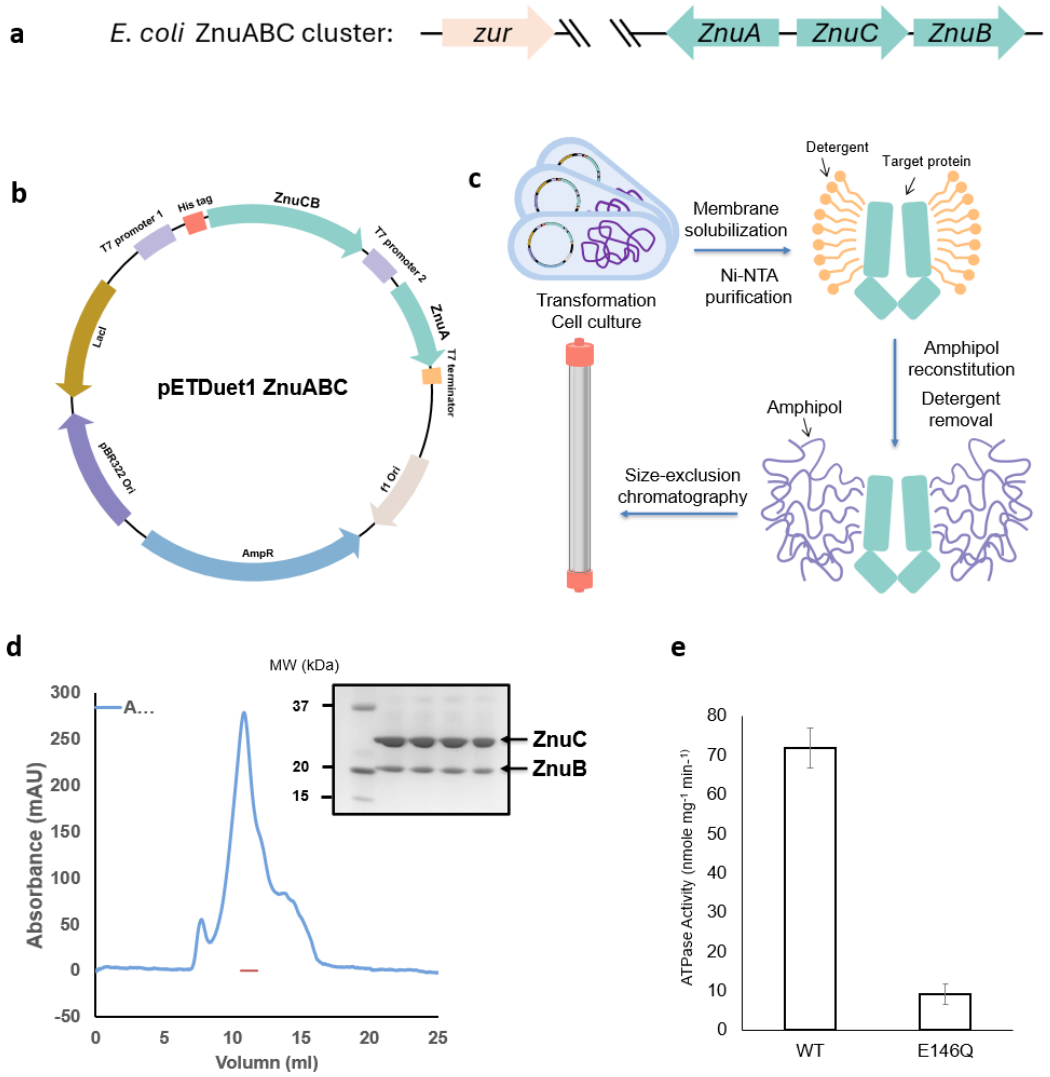

Fig. S1. Expression and purification of the ZnuB-ZnuC complex. **a**, *Escherichia coli ZnuABC* gene cluster regulated by the *zur* regulon. **b**, Construction of pETDuet-ZnuABC plasmid for expression of ZnuB-ZnuC. **c**, Workflow of protein purification and reconstitution to amphipol nanodiscs. **d**, Size-exclusion chromatography (SEC) peak profile and SDS-PAGE analyses of the reconstituted ZnuB-ZnuC in amphipol A8-35**.** The lanes are eluted fractions from size-exclusion chromatography indicated by a red line. **e**, ATPase activity of the purified wild-type ZnuB-ZnuC and its E146Q mutant. Error bar indicates the standard deviation (S.D.) from three repeats.

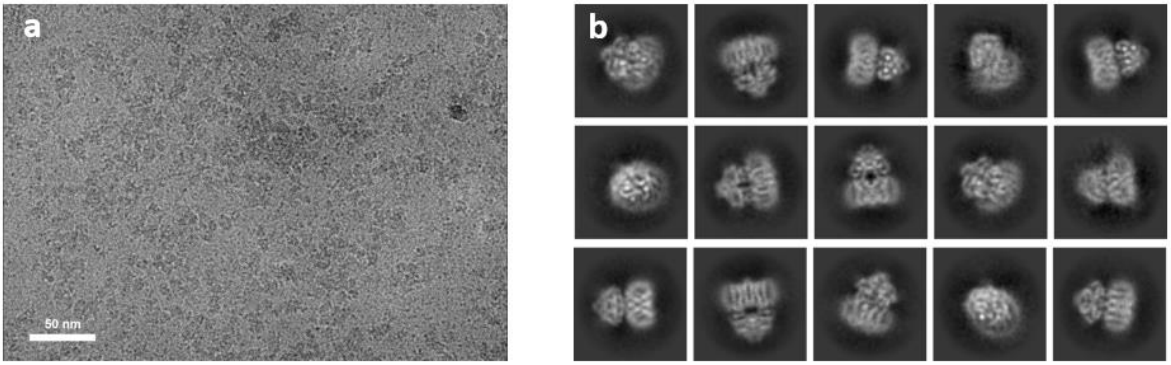

Fig. S2. CryoEM structure determination for the AMP-PNP state ZnuBC. **a**, A typical motion-corrected cryo-EM micrograph from a total of 5283 micrographs. Each particle is a 2D projection and alone does not provide adequate resolution for a high-resolution 3D structure. **b**, Selected views of 2D class averages.

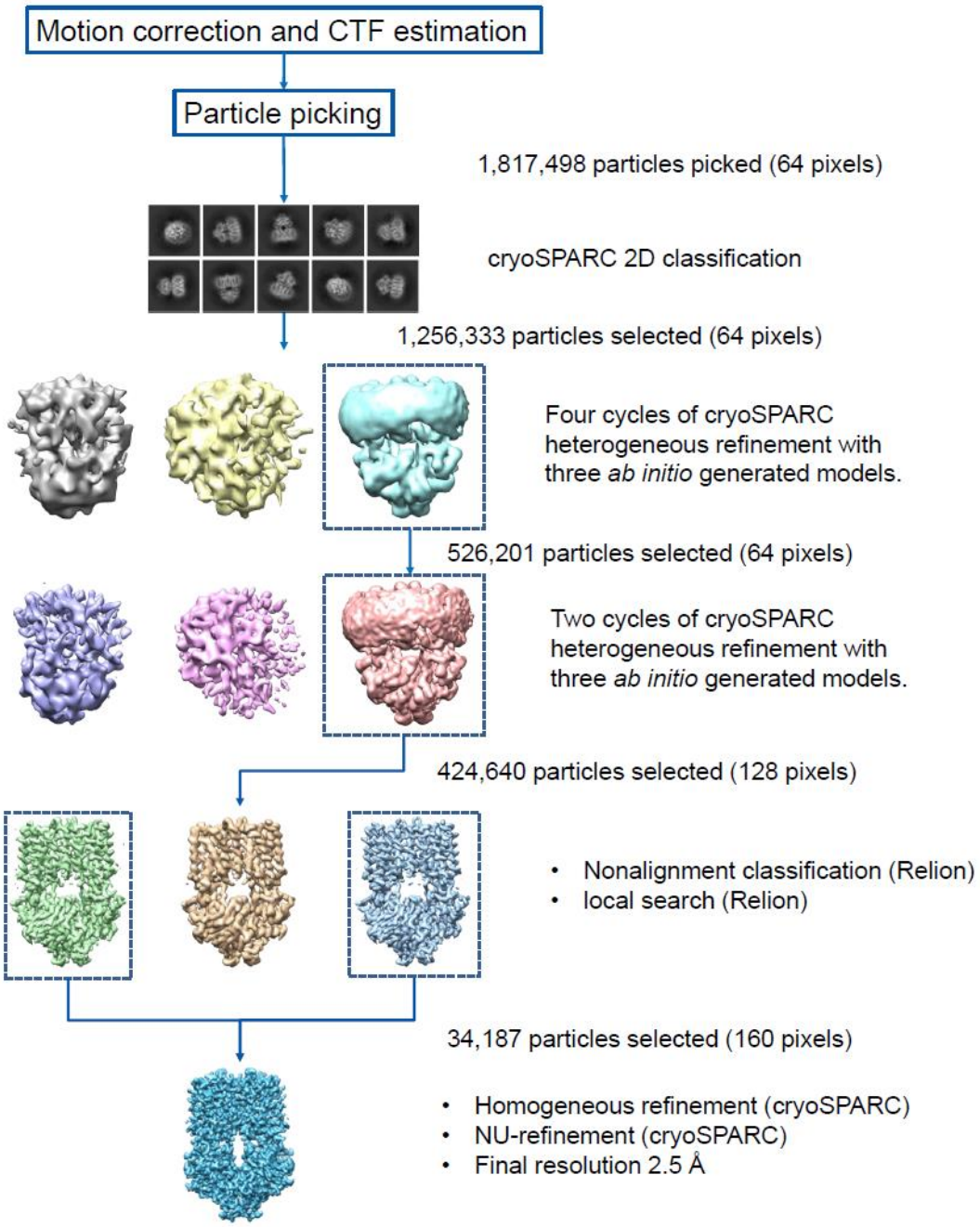

Fig. S3. Representative data analysis workflow for the reconstruction of the ZnuBC structure. The workflow shown here is for AMP-PNP state. Other reconstructions used a similar workflow.

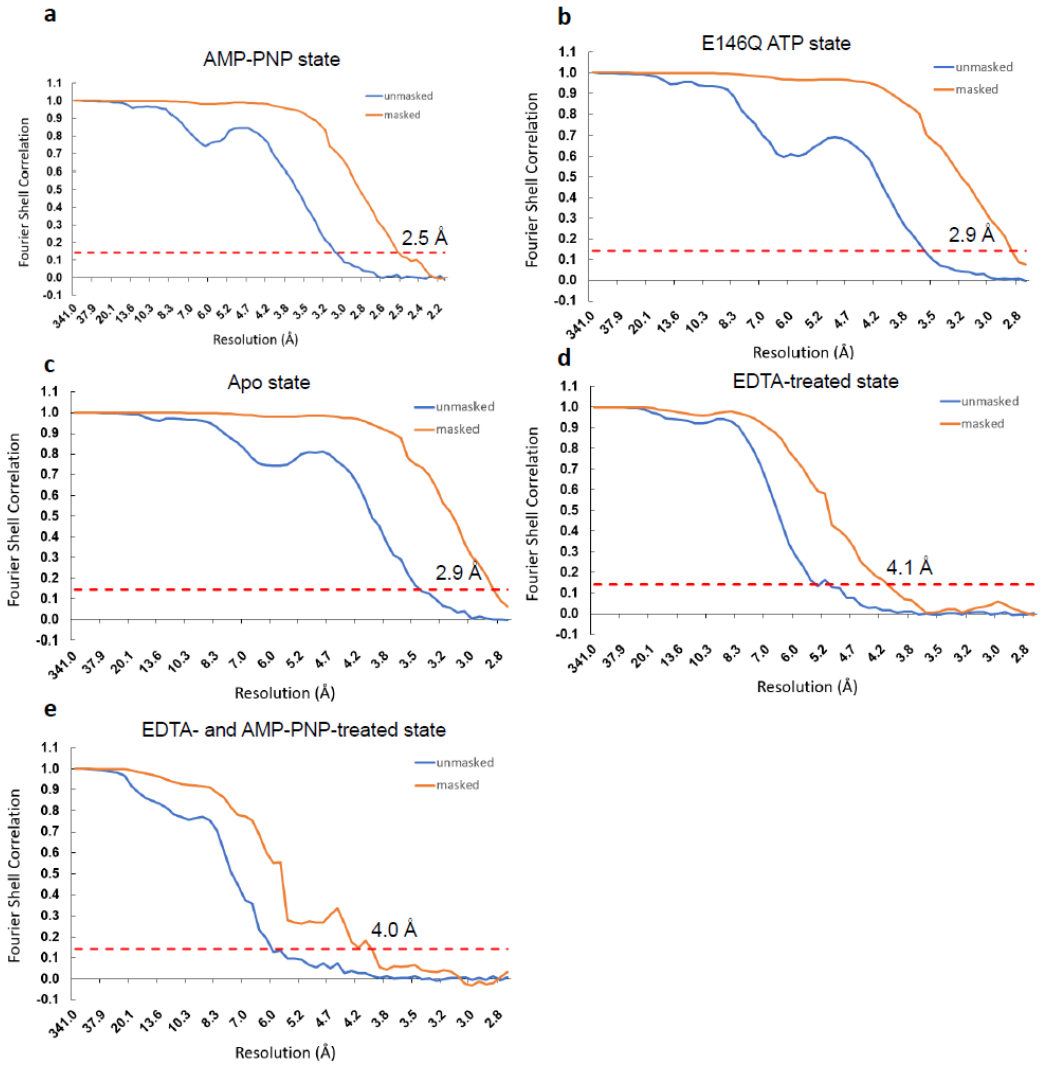

Fig. S4. Fourier shell correlation (FSC) curves for the unmasked and masked 3D reconstructions of ZnuBC in various states. a, AMP-PNP state. **b**, E146Q ATP state. **c**, Apo state. **d**, EDTA-treated state. **e**, EDTA- and AMP-PNP-treated state.

Fig. S5.

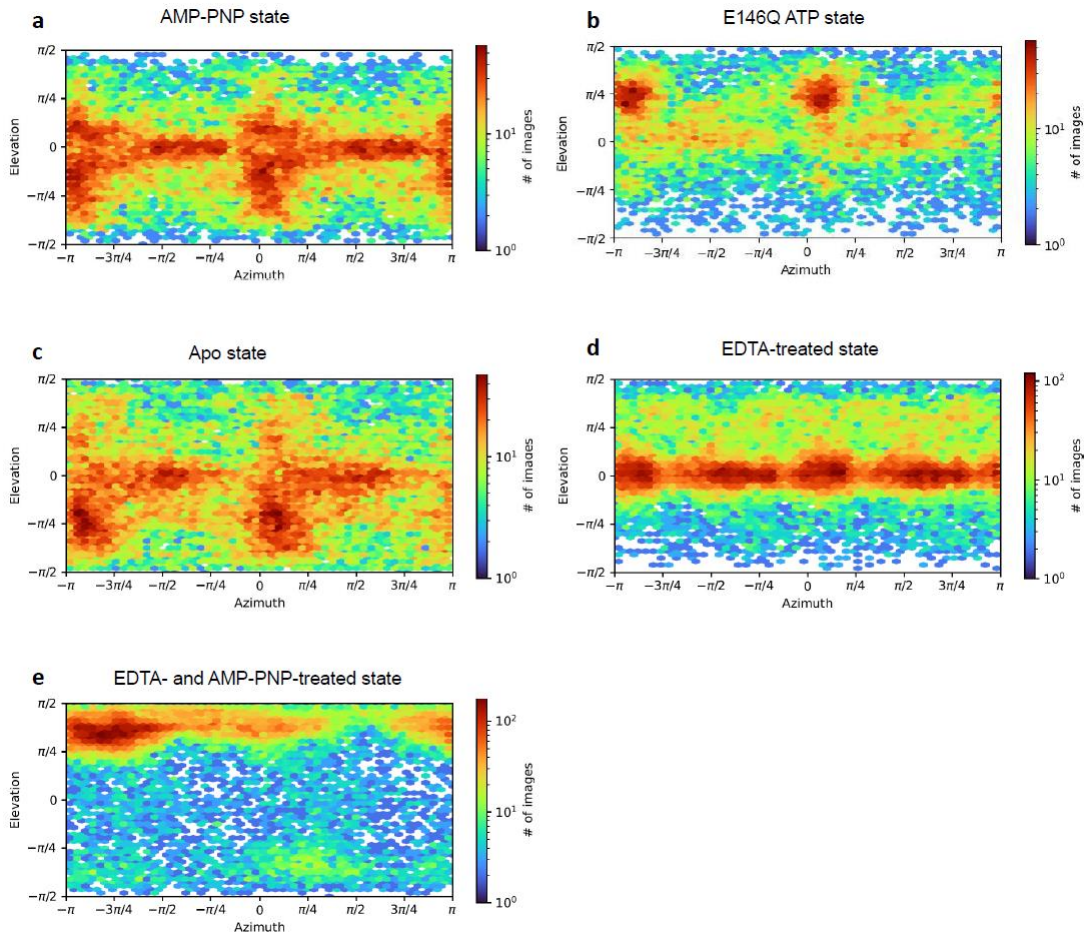

Orientation distribution for particles used in the 3D reconstructions of ZnuB-ZnuC in various states. **a**, AMP-PNP state. **b**, E146Q ATP state. **c**, Apo state. **d**, EDTA-treated state. **e**, EDTA- and AMP-PNP-treated state.

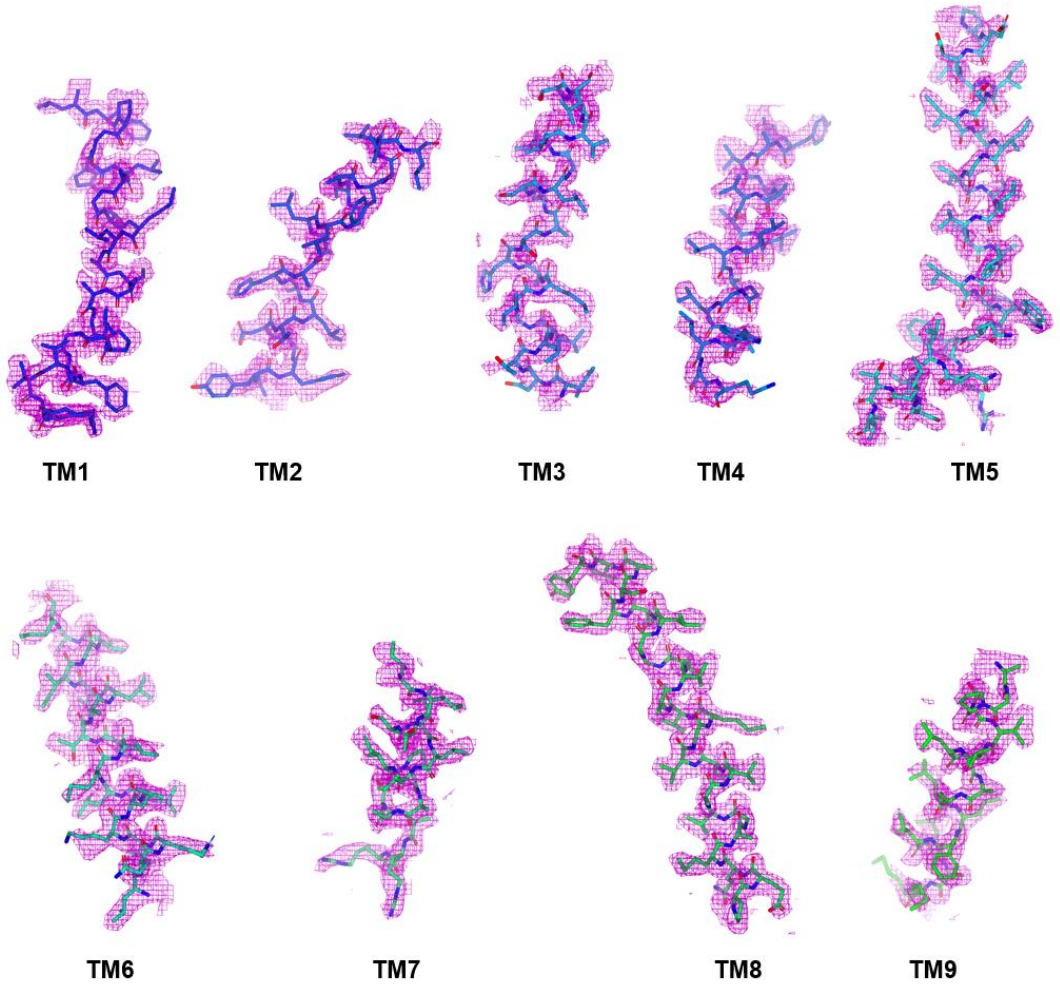

Fig. S6 CryoEM densities for the nine transmembrane helices in a ZnuB subunit (AMP-PNP state) to show the quality of the map. The densities are shown as magenta isomeshes contoured at 7σ. Transmembrane helices are shown as sticks.

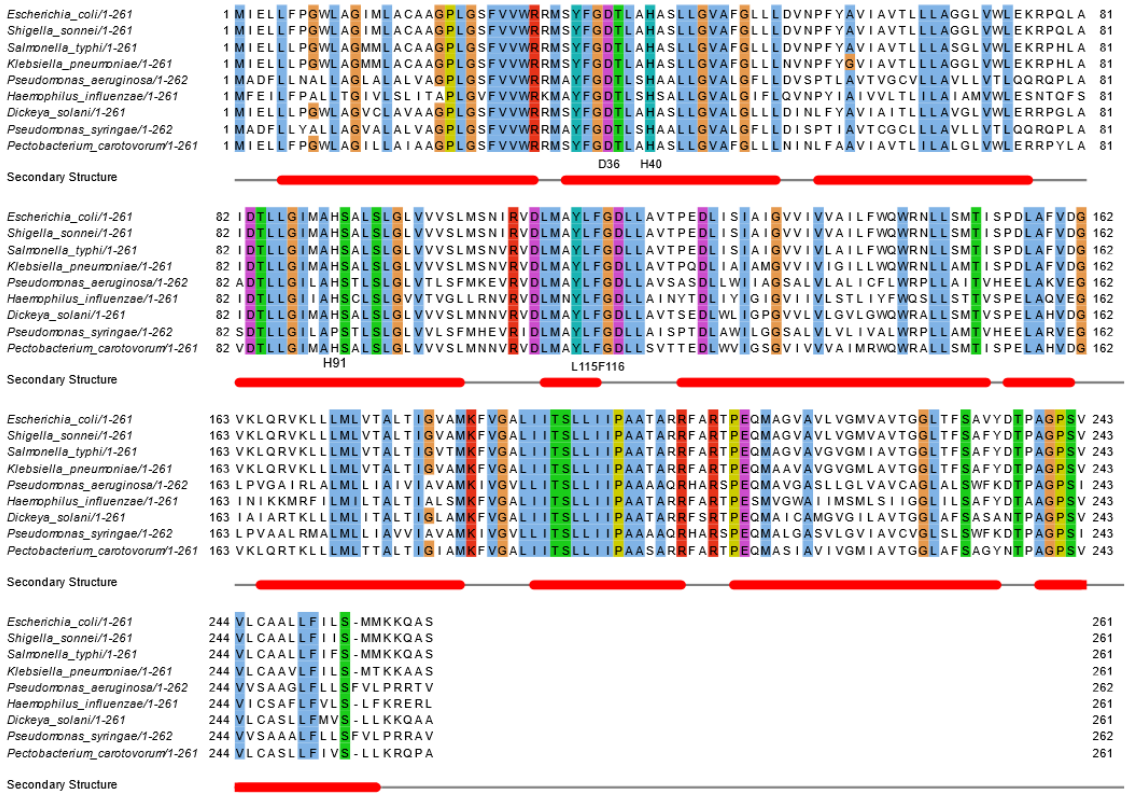

Fig. S7. Sequence alignments of ZnuBs from pathogens. Conserved residues Asp36 and His40 and less conserved residue His91 are indicated. The residue numbering is for *Escherichia coli* ZnuB**.** UniProt (https://www.uniprot.org/) numbers used for sequence alignments are P39832 from *Escherichia coli*, Q3Z2L7 from *Shigella sonnei*, Q8Z5W5 from *Salmonella typhi*, A0A486TZB0 from *Klebsiella pneumoniae*, Q9HT72 from *Pseudomonas aeruginosa*, P44691 from *Haemophilus influenzae*, UniRef100_UPI002930D2B9 from *Dickeya solani*, Q87UN1 from *Pseudomonas syringae*, C6DFF7 from *Pectobacterium carotovorum.*

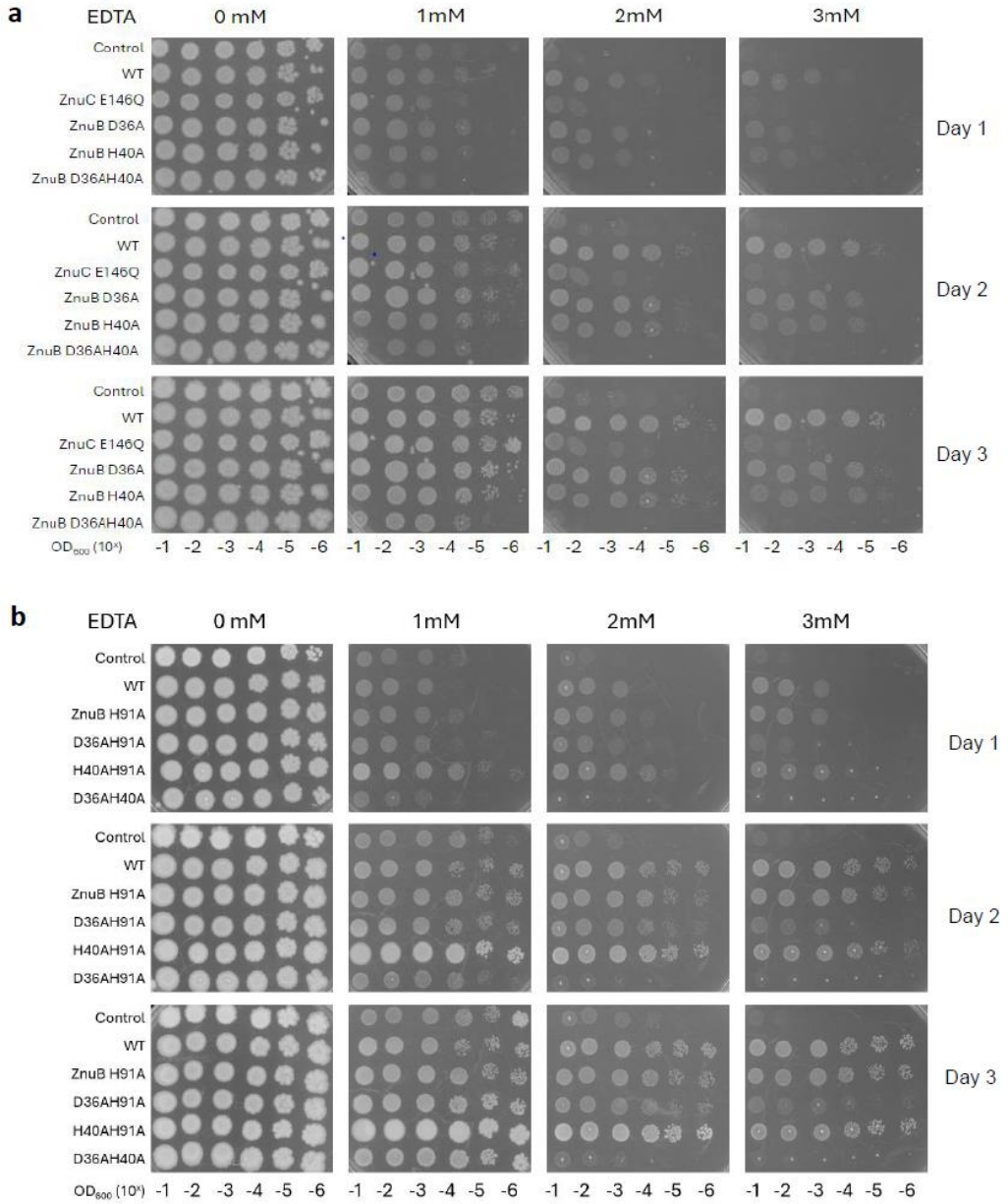

Fig. S8. Cell growth viability essays of ZnuB-ZnuC wild-type and mutants. *E. coli* C43 cells were transformed with indicated plasmids for plating Argar-LB plates with indicated EDTA and the presence of 0.2 mM IPTG (final). Prior to plating, cells were diluted to the indicated OD_{600} values. The cell growth was monitored on day 1, day 2, and day 3. **a**, Cell growth viability for ZnuB Asp36 and His40 mutants. Compared with the control which has an empty plasmid, D36A-H40A double mutant and E146Q ATPase inactive mutant (ZnuC) showed increased cell toxicity with externally added EDTA concentration at 2 or 3 mM. **b**, Cell growth viability for ZnuB His91 mutants. H91A didn't show increased cell toxicity compared to the WT, suggesting its less essential role in zinc uptake. s

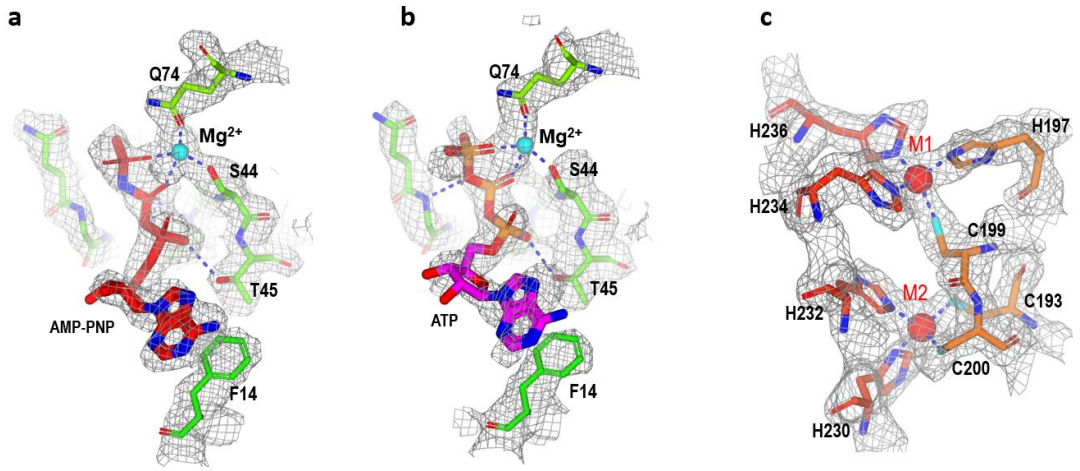

Fig. S9. CryoEM densities for AMP-PNP, E146Q-ATP, and two Zn^{2+}-binding sites. The densities are shown as gray isomeshes contoured at 7σ. AMP-PNP and ATP molecules are shown as sticks. Hydrogen bond interactions are shown as dashed blue lines. Mg^{2+}, cyan spheres; Zn^{2+}, red spheres. **a**, AMP-PNP site. **b**, ATP site. **c**, Two Zn^{2+} binding sites at the C-terminus of ZnuC.

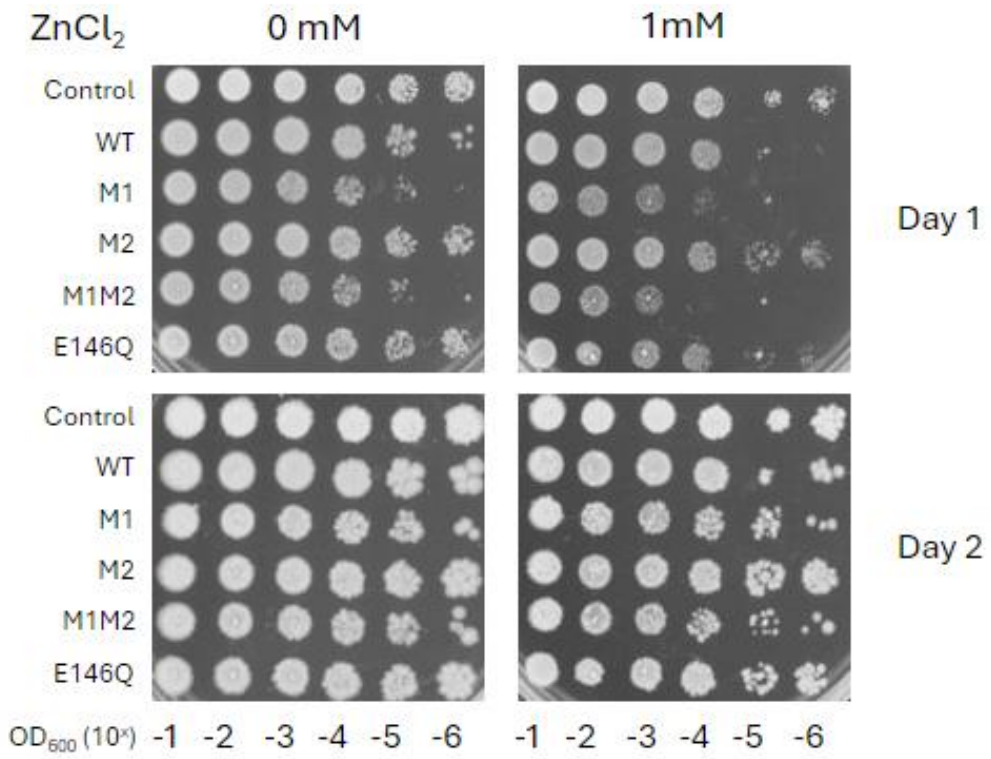

Fig. S10 Cell growth viability assays of ZnuB-ZnuC wild-type and mutants. *E. coli* C43 cells transformed with indicated plasmids for plating Argar-LB plates with buffer or 1 mM Zn^{2+} and the presence of 0.2 mM IPTG (final). Prior to plating, cells were diluted to the indicated OD_{600} values. The cell growth was monitored on day 1 and day 2. Compared with the control which has an empty plasmid, M1 or M1-M2 double mutants in ZnuC showed cell toxicity.

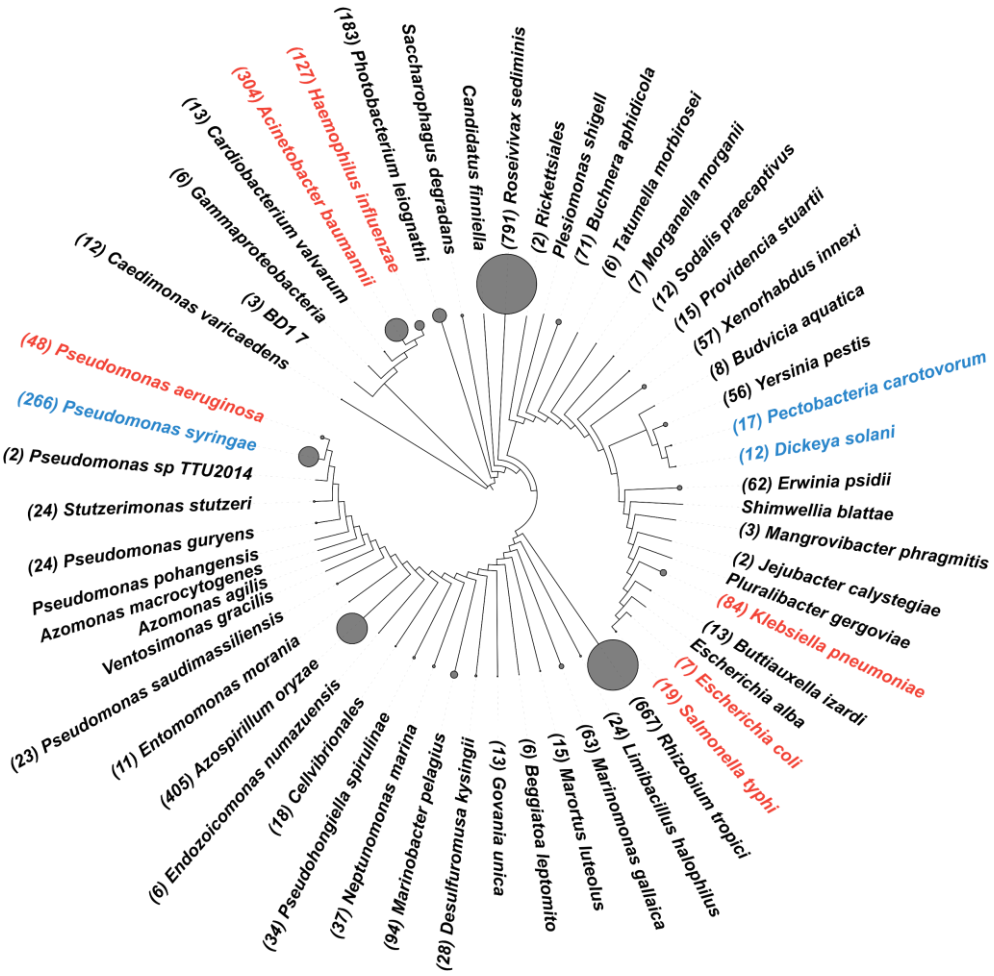

Fig. S11. A cladogram of ZnuCs containing the CxxxHxCCxGxP motif. The multiple sequence alignment and neighbor-joining tree were conducted in MEGA11 with default settings(*49*). Numbers in the bracket indicate the number of leaves of that branch. Human pathogens are colored *red*; plant pathogens are colored *blue*. The bacterial tree of life shows that ZnuC homologs are found in most bacterial lineages, encompassing 1,572 representative bacteria from 23 different phyla. The cladogram is prepared using iTOL (https://itol.embl.de/).

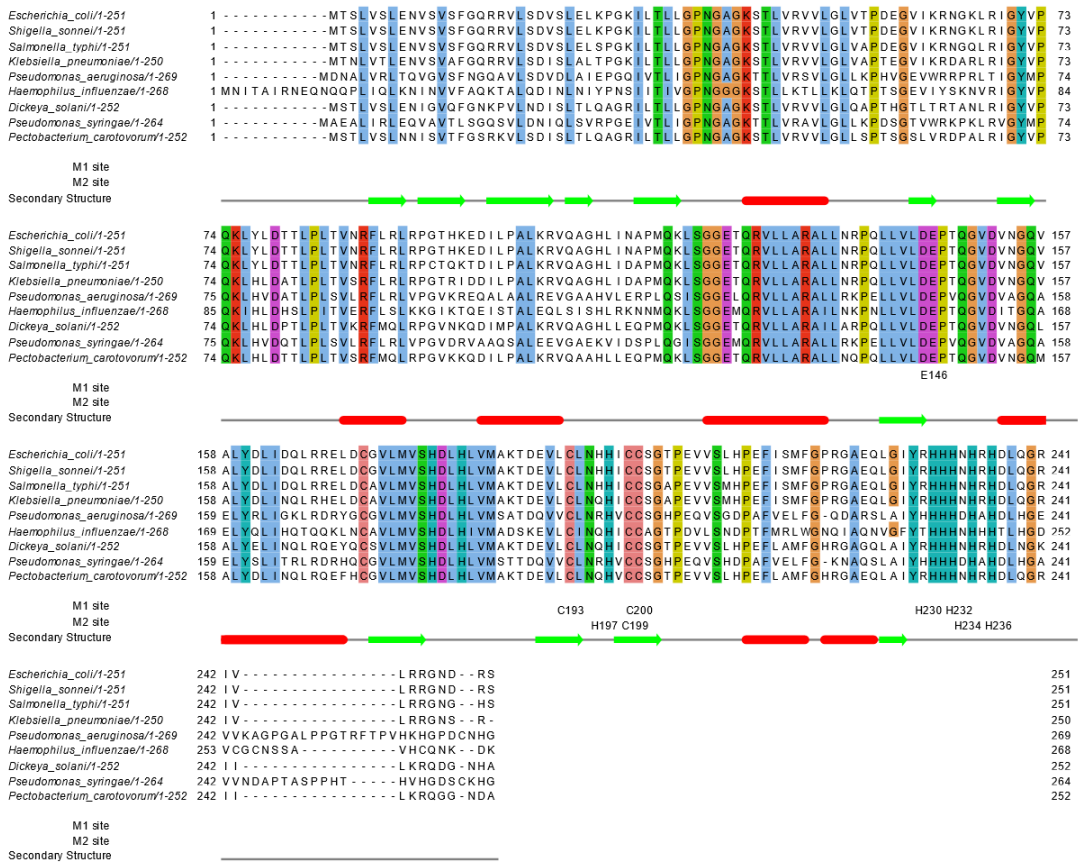

Fig. S12. Sequence alignments of ZnuC from pathogens. The residues that coordinate the M1 and M2 sites are indicated. The residue numbering is for *E. coli* ZnuC**.** UniProt (https://www.uniprot.org/) numbers used for sequence alignments are P0A9X1 from *Escherichia coli*, Q3Z2L6 from *Shigella sonnei*, Q8Z5W6 from *Salmonella typhi*, A0A483GJV2 from *Klebsiella pneumoniae*, Q9HT73 from *Pseudomonas aeruginosa*, P44692 from *Haemophilus influenzae*, A0A2K8VTG0 (UniRef100_UPI0003A98390) from *Dickeya solani*, Q87UN0 from *Pseudomonas syringae*, C6DFF8 from *Pectobacterium carotovorum.*

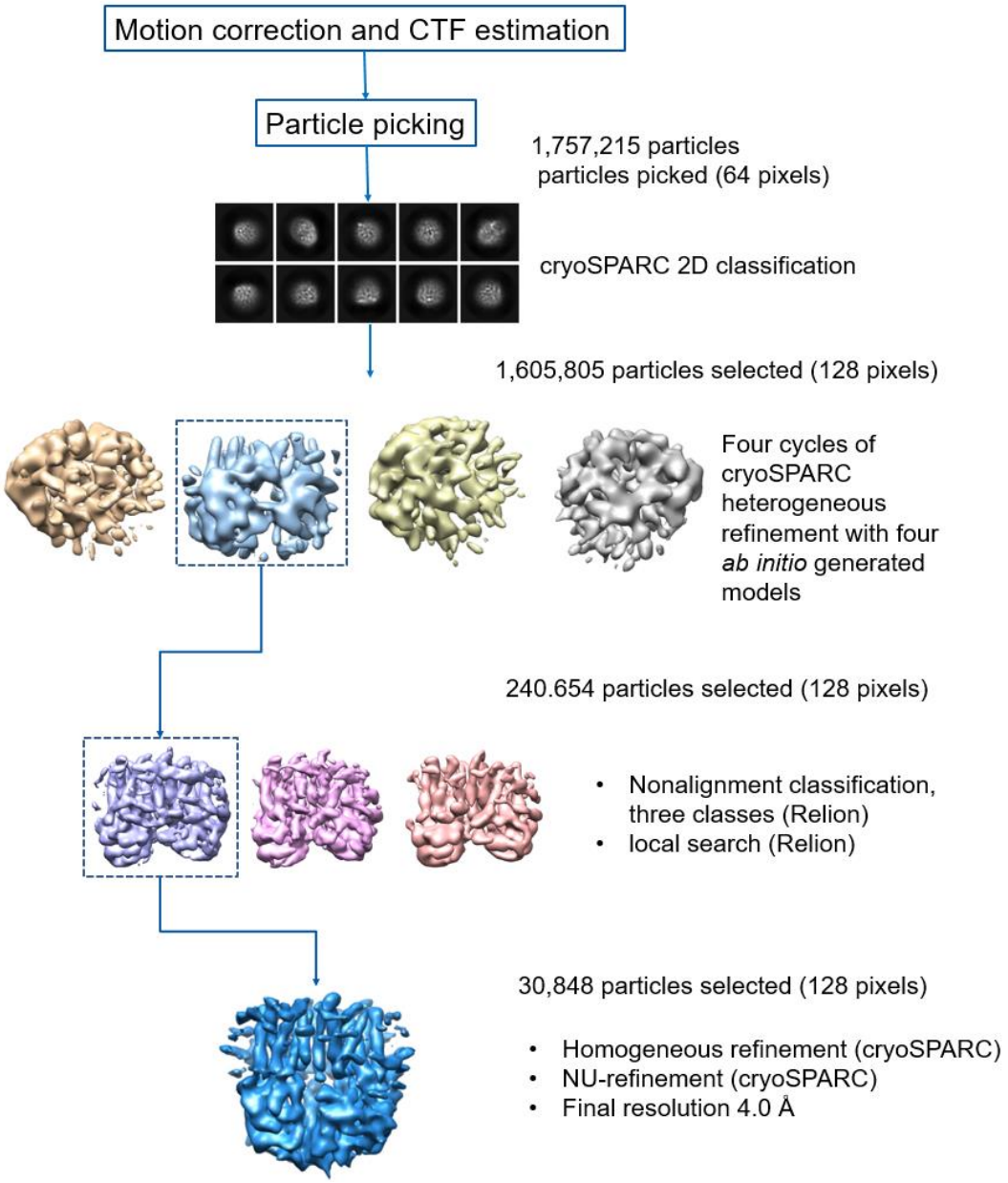

Fig. S13. Data analysis workflow for the reconstruction of the ZnuBC structure treated by EDTA and AMP-PNP.

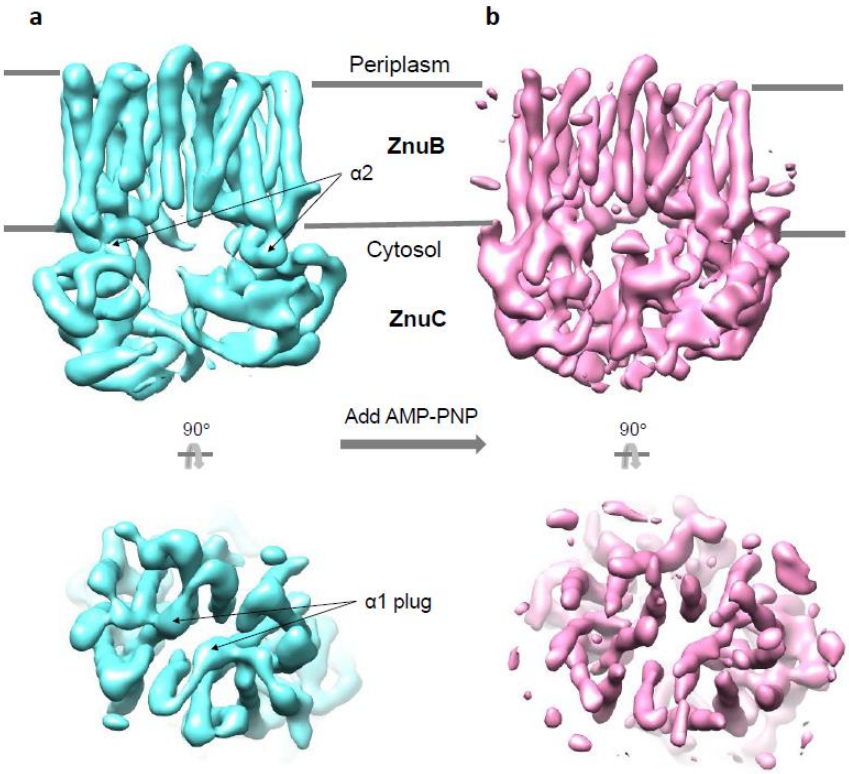

Fig. S14. Comparison of cryoEM densities for EDTA-treated structure (a) and EDTA/AMP-PNP-treated structure (b). In the EDTA-treated structure, the regions for helices α1 and α2 on ZnuB are indicated. Adding AMP-PNP caused the contraction of ZnuC toward ZnuB, which pushes α2 and triggers conformational changes in ZnuB, including disordering of α1, the sealing plug.

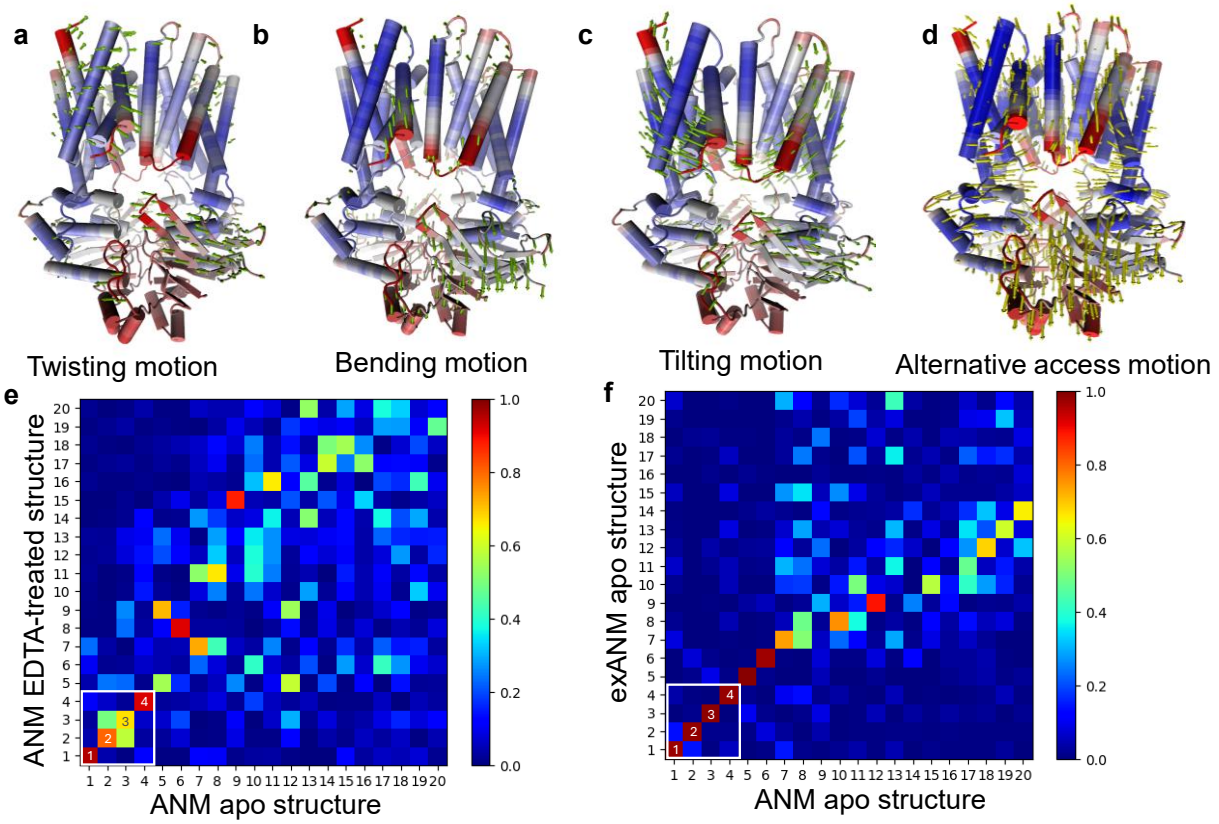

Fig. S15. Anisotropic network model analysis of the collective dynamics of the ZnuBC complex structures. a-d, Motions in the first four ANM modes shown in **e**. **a**, ANM1, twisting motion. **b**, ANM2, bending motion. **c**, ANM3, tilting motion. **d**, ANM4, alternative access motion. ANM modes 1-3 are the mostly rigid-body motions in the ZnuB transporter domain, and ANM4 shows conformational changes in the ZnuB transporter domain, consistent with an alternative access transport model. **e**, Correlation between the 20 lowest-frequency ANM modes of motion computed for the apo and the EDTA-treated structures. **f**, Correlation between the 20 modes computed for the apo structure alone and that in the presence of explicit membrane (exANM). The entries represent the correlation cosines between the modes of motion, varying from 0 to 1 with 0 meaning no correlation and 1 means completely correlated and is color-coded from blue to red, accordingly.

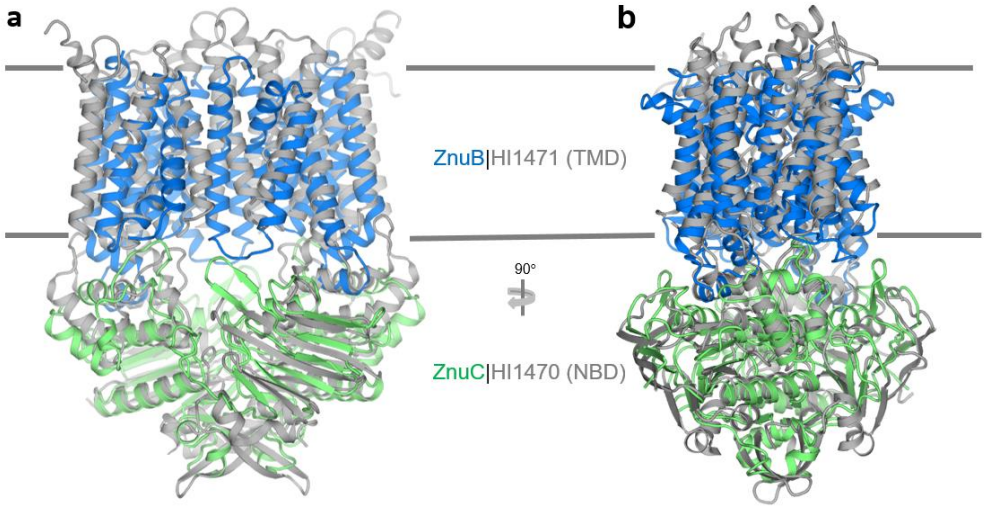

Fig. S16. Two cartoon views of the structural alignment of inward-facing type II ABC transporter HI1471/0 with inward-facing ZnuBC model from ANM 4. The alignment RMSD is 3.92 Å for 753 aligned Cα atoms from TMD and NBD domains. ZnuB is marine, ZnuC is green, and HI1471 and HI1470 are gray.

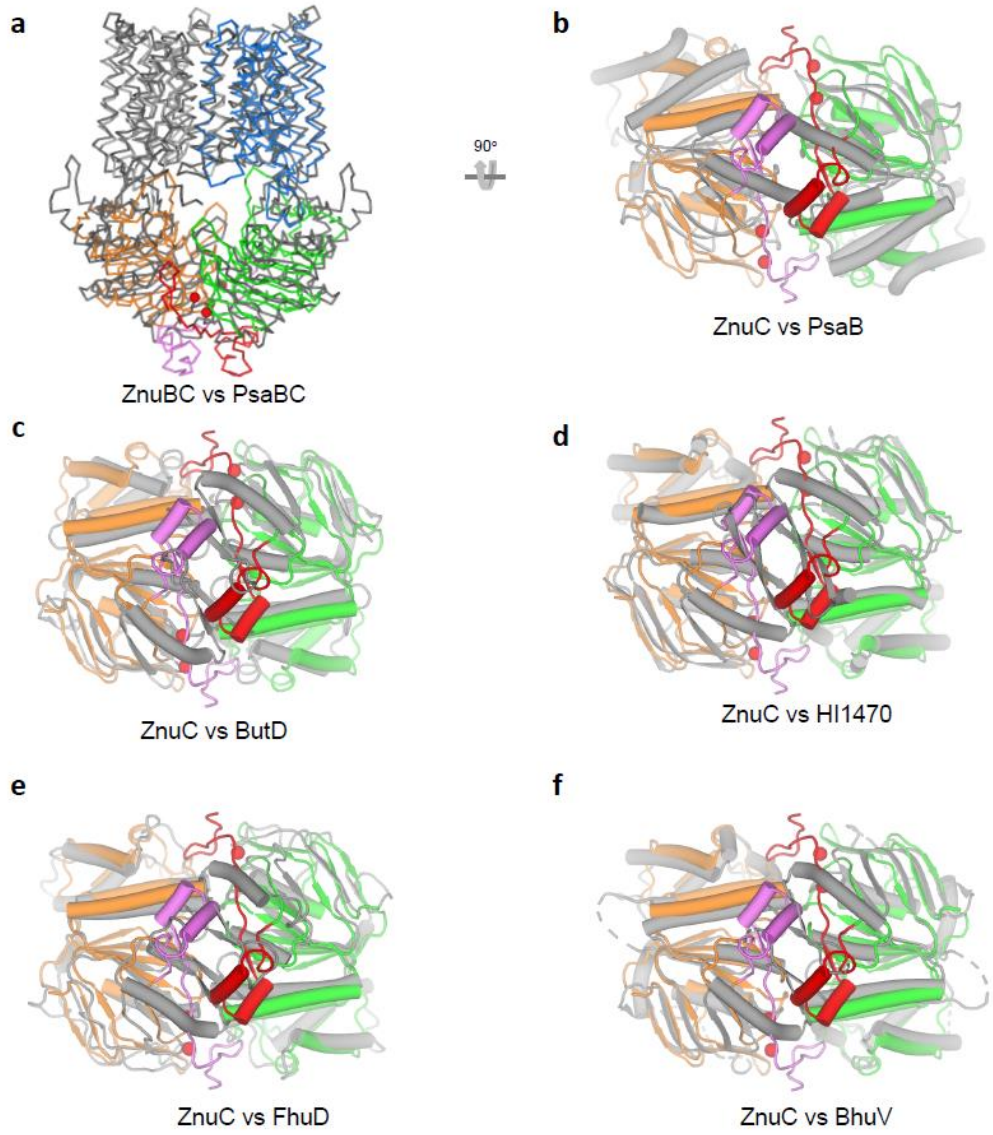

Fig. S17. Comparison of ZnuC with the NBDs of other type II ABC transporters. (**a**) Superimposition of ZnuBC with PsaBC (PDB code 7KYP) structure are shown as ribbons. ZnuBC is colored gray and marine for ZnuB, orange and green for ZnuC NBD domains, and magenta and red for the ZnuC ZSD domains. The comparison of ZnuC (colored in orange, magenta, green, and red) with other type II ABC transporter NBDs (colored in gray) are shown as cartoons for PsaB (**b**), ButD (**c**), HI1470 (**d**), FhuD (**e**), and BhuV (**f**).

Table S1. Primer sequences used in this work.

Primer name	Sequence (from 5' to 3')
ZnuCB BamHI forward	GCCAGGATCCGAATTCACAAGTCTGGTTTCCCTGGA
ZnuCB HindIII reverse	GGCGAAGCTTTTAGCTGGCCTGCTTTTTCA
ZnuA NdeI forward	TATACATATGTTACATAAAAAAACGCTTCT
ZnuA XhoI reverse	CAGACTCGAGATCTCCTTTCAGGCAGCTCG
M13F	GTAAAACGACGGCCAGTG
M13R	GGAAACAGCTATGACCATG
pET upstream primer forward	ATGCGTCCGGCGTAGA
DuetUP2 primer	TTGTACACGGCCGCATAATC
DuetDown1 primer reverse	GATTATGCGGCCGTGTACAA
T7 terminator primer	GCTAGTTATTGCTCAGCGG
ZnuC E146Q forward	AGTGCTGGATCAGCCCACTCAAG
ZnuC E146Q reverse	AATAATTGCGGGCGATTTAAC
ZnuB D36A forward	TTATTTCGGTGCGACGCTGGCTC
ZnuB D36A reverse	GACATACGACGCCAG
ZnuB H40A forward	TACGCTGGCTGCGGCCTCATTACTTG
ZnuB H40A reverse	TCACCGAAATAAGACATAC
ZnuB H40AD36A forward	GACGCTGGCTGCGGCCTCATTACTTG
ZnuB H40AD36A reverse	GCACCGAAATAAGACATAC
ZnuC C193A C200A forward	CACATTTGTGCTTCCGGCACACCGGAAG
ZnuC C193A C200A reverse	GTGATTCAGGGCCAGCACTTCATCGGTTTTTGC
ZnuC H230A H232A forward	ATGCTAACCATCGTCACGATTTAC
ZnuC H230A H232A reverse	GAGCGCGATAGATACCCAGTTG
ZnuC H197A C199A forward	TTGCTTGTTCCGGCACACCG
ZnuC H197A C199A reverse	TGGCGTGATTCAGGCACAGCAC
ZnuC H234A H236A forward	GTGCCGATTTACAGGGACGAATTG
ZnuC H234A H236A reverse	GAGCGTTATGATGATGGCGATAG
ZnuC C193A H197A C199A C200A forward	GCCATTGCTGCTTCCGGCACACCGGAAG
ZnuC C193A H197A C199A C200A reverse	GTGATTCAGGGCCAGCACTTCATCGGTTTTTGC
ZnuC H240A H242A H244A H246A forward	ACGCTCGTGCCGATTTACAGGGACGAATTG
ZnuC H240A H242A H244A H246A reverse	TAGCATGAGCGCGATAGATACCCAGTTG

Table S2. CryoEM data collection, 3D reconstruction, and refinement statistics.

Data Collection	AMP-PNP	E146Q ATP	Apo	EDTA-treated	EDTA-treated, AMPNP
Microscope	Krios G3i	Krios G3i	Krios G3i	Krios G3i	Krios G3i
Magnification	130 Kx	130 Kx	130 Kx	130 Kx	130Kx
Stage type	Autoloader	Autoloader	Autoloader	Autoloader	Autoloader
Voltage (kV)	300	300	300	300	300
Detector	Gatan K3	Gatan K3	Gatan K3	Gatan K3	Gatan K3
Energy filter (eV)	15	15	15	15	15
Acquisition mode	Super-resolution	Super-resolution	Super-resolution	Super-resolution	Super-resolution
Physical pixel size (Å)	0.666	0.666	0.666	0.666	0.666
Defocus range (μm)	0.7-2.3	0.7-2.3	0.7-2.3	0.7-2.3	0.9-2.3
Electron exposure (e^-/Å^2)	66	66	66	66	66
Reconstruction					
Software	Relion v3.08, cryoSPARC v3.2.0	Relion v3.08, cryoSPARC v3.2.0	Relion v3.08, cryoSPARC v3.2.0	Relion v3.08, cryoSPARC v3.2.0	Relion v3.08, cryoSPARC v3.2.0
Particles picked	1,817,498	125,0170	1,366,732	3,590,067	1,757,215
Particles final	34,187	18,325	32,554	44,314	30,846
Extraction box size (pixels)	256	256	256	256	256
Rescaled box size (pixels)	160	128	128	128	128
Final pixel size	1.066	1.332	1.332	1.332	1.332
Symmetry imposed	C2	C2	C2	C1	C1
Map resolution (Å)	2.5	2.9	2.9	4.1	4.0
FSC threshold	0.143	0.143	0.143	0.143	0.143
Map resolution range (Å)	341-2.50	341-2.9	341-2.9	341-4.1	341-4.0
Model refinement					
Software	PHENIX	PHENIX	PHENIX	PHENIX	
Refinement algorithm	Real Space	Real Space	Real Space	Real Space	
Clipped box size (pixels)	None	None	None	None	

Number of residues	998	994	998	910
Number of Zn^{2+}	4	4	4	0
Number nucleotide	2	2	0	0
R.M.S. deviations				
Bond length (Å)	0.005	0.004	0.002	0.006
Bond angle (°)	0.644	0.596	0.470	0.898
Molprobity clashscore	2.71	2.02	2.91	13.16
Rotamer outliers (%)	0.0	0.0	0.0	0.0
Cβ deviations (%)	0.0	0.0	0.0	0.0
Ramachandran plot				
Favored (%)	98.20	99.19	97.60	94.51
Allowed (%)	1.80	1.81	2.40	4.84
Outliers (%)	0.0	0.0	0.0	0.66
PDB code	9OKO	9OKP	9OKQ	9OKR

Movie S1: Movie visualization of ANM mode 1

Movie S2: Movie visualization of ANM mode 2

Movie S3: Movie visualization of ANM mode 3

Movie S4: Movie visualization of ANM mode 4